Exploring Hyperfine Coupling in Molecular Qubits

Joan Cardona,[a] Àlex Solé,[a,b] Pablo Mella,[c] Daniel Aravena,[c]* Javier Ruiz-Hidalgo,[b]* Silvia Gómez-Coca[a*] and Eliseo Ruiz[a]*

Received 00th January 2025,
Accepted 00th January 2025

DOI: 10.1039/x0xx00000x

Molecular qubits represent a promising avenue for advancing quantum sensing and computing technologies, yet significant challenges remain in optimising their performance. Hyperfine coupling critically influences molecular qubit coherence, creating substantial interactions between the qubit and its environment that dramatically reduce coherence time. While previous studies have exhaustively investigated this phenomenon, a comprehensive understanding of the underlying mechanisms across different systems remains elusive. A benchmark test was performed using DFT to assess which methodology worked best to accurately predict hyperfine coupling constants in molecular qubits predominantly composed of V^{IV} and Cu^{II}. We systematically analysed the decomposition of hyperfine coupling and examined how variations in coordination sphere and molecular geometry impact dipolar, isotropic and spin-orbit contributions. By modelling diverse systems, we demonstrate how molecular design can fine-tune hyperfine coupling contributions, either minimising overall interaction or enhancing coupling along specific axes. This study provides useful insights into the structure-property relationships governing hyperfine coupling mechanisms and assesses the accuracy of different choices of density functional, basis sets and relativistic corrections in the prediction of hyperfine coupling constants.

Introduction

Magnetic molecules play a prominent role in quantum devices due to their electronic spin behaviour, making them potential candidates as qubits and quantum sensors.[1-4] A variety of two-state systems have been explored as potential platforms for qubit realisation, benefiting from different physical implementations such as photons,[5] electronic spins,[6] trapped ions,[7] ultracold atoms,[8] superconductor Josephson junctions,[9] and quantum dots.[10] Electronic spins can directly behave as qubits, and controlling their direction is a fundamental element in achieving sufficiently long coherence times for technological applications.[2,11] Currently, diamond NV centres are being implemented in technological devices, mainly for quantum sensing. These systems are employed in scanning probe microscopy or single-photon emitters despite the difficulty of controlling the concentration of spin centres and the behaviour of such defects. In this way, magnetic molecules present a great potential to be competitive with NV centres if coherence times can be improved, as molecular crystals can be designed to yield an ordered array of spin centres, avoiding the problems associated with qubits based on randomly distributed defects. [12, 13]

Quantum coherence represents a critical parameter for qubit performance, with coherence times necessarily exceeding gate operation timescales (0.1-1ms) to facilitate fault-tolerant quantum computation.[14] Measuring coherence time is experimentally carried out using pulsed Electron Paramagnetic Resonance (EPR), which is a highly specific technique that involves a Hahn echo pulse[15] to study the dephasing of electron spins. Furthermore, the level of complexity and resources required to obtain most qubits is very high; hence, molecular spin-based qubits are an attractive alternative. They offer great tunability,[16, 17] homogeneity in comparison with the defects of solid-state spin qubits, and easy enough synthetic approaches. However, they still face the same challenge of maintaining coherence over spin-lattice (T_1) and spin-spin (T_2) relaxation mechanisms. The former involves vibrational relaxation of the lattice, while the latter centres on interactions between spins, both contributing to dephasing.[18] At lower temperatures, the limiting factor is T_2 due to reduced molecular vibrations from insufficient thermal energy; on the other hand, when higher temperatures are reached, T_1 decreases exponentially, and it becomes the main hindrance due to efficient spin-phonon coupling.[19]

Hyperfine Coupling (HFC) between electron and nuclear spins introduces additional spin interactions that can significantly contribute to the T_2 relaxation mechanisms, especially in the low-temperature regime.[3, 18] This interaction arises from the magnetic coupling between the electron spin and the nuclear spin(s) of the same atom (hyperfine) or nearby atoms (superhyperfine).[20] The Spin Hamiltonian approach is often employed to study these interactions systematically. In this formulation, the energy spectrum is projected

---

[a] Departament de Química Inorgànica i Orgànica and Institut de Recerca de Química Teòrica i Computacional, Universitat de Barcelona, Diagonal 645, 08028 Barcelona, Spain.
[b] Department of Image Processing Group - Signal Theory and Communications Department, Universitat Politècnica de Catalunya, Jordi Girona 1-3, 08034 Barcelona, Spain.
[c] Departamento de Química de los Materiales, Facultad de Química y Biología, Universidad de Santiago de Chile, Casilla 40, Correo 33, Santiago, Chile.

† Footnotes relating to the title and/or authors should appear here.

Supplementary Information available: [details of any supplementary information available should be included here]. See DOI: 10.1039/x0xx00000x

to the small, low-energy manifold, which is important to the magnetic properties of the system, as expressed in equation 1.[20, 21]

$$\hat{H}_{\text{spin}} = \hat{S}\mathbf{D}\hat{S} + \mu_B \boldsymbol{g}\mathbf{B}\hat{\mathbf{S}} + \sum_A \hat{\mathbf{S}}\mathbf{A}^{(A)}\hat{\mathbf{I}}^{(A)} \tag{1}$$

Here, the first term is attributed to the Zero-Field Splitting (ZFS) which describes the interactions resulting from the presence of more than one unpaired electron, where $\hat{S}$ is the operator for the electron spin and $\mathbf{D}$ describes the spin-spin interaction between two or more unpaired spins. The second term represents the electronic Zeeman effect (where μ_B is Bohr magneton, $\boldsymbol{g}$ is the electron g-factor and $\mathbf{B}$ is the applied magnetic field). For a free electron, the g-factor is approximately 2.0023. However, in chemical systems, the g-factor can vary significantly due to spin-orbit coupling and other interactions. The magnetic anisotropy described by the g-factor offers detailed information about the spatial arrangement and geometry of the metal complex. In anisotropic systems, such as those with low symmetry or strong ligand fields, the g-factor becomes directionally dependent, reflecting the interaction between the unpaired electron magnetic moment and the local environment. Finally, the third term represents the HFC (where $\mathbf{A}^{(A)}$ is the hyperfine tensor and $\hat{\mathbf{I}}^{(A)}$ is the nuclear spin for a nucleus *A*).

Recent molecular qubit studies[19, 22] seem to point towards mononuclear complexes based on *S*=1/2 systems as potential candidates for molecular systems with long coherence time. To avoid spin-spin interactions, we have chosen first-row transition metals, V^{IV} and Cu^{II}, as they present d^1 and d^9 electronic configurations and reported the best coherence times.[4, 6, 23-25] Longer coherence times have also been achieved through ligand design by favouring spin-free nuclei, reducing electronic-nuclear spin interactions.[26] Beyond minimising spin-spin interactions, a ligand should also possess rigidity to minimise vibrational perturbations, thereby reducing spin-phonon coupling.[3, 27, 28]

In recent advances within quantum computing materials, understanding the fundamental principles governing molecular spin qubits has become increasingly crucial.[29] This research addresses a significant gap in our understanding of these systems. This work aims to understand how to modulate HFC in copper and vanadium compounds to develop systems with enhanced coherence. This investigation led us to evaluate various computational methods to identify a precise approach for calculating the hyperfine coupling constant $\mathbf{A}$. Through this methodology, we analysed the geometric and electronic factors that determine the HFC constants, ultimately providing insights into how this parameter can be effectively modulated for optimal qubit performance.

Hyperfine Coupling Contributions

The theoretical framework presented in this section draws on established equations from the literature.[20, 21] The HFC interaction ($\text{A}_{\mu\nu}^{(A)}$) can be decomposed by considering the isotropic, also called Fermi contact, ($\text{A}_{iso}^{(A)}$), dipolar ($\text{A}_{\mu\nu}^{(A;dip)}$) and the spin-orbit contributions ($\text{A}_{\mu\nu}^{(A;SOC)}$). This term is treated as a 3x3 tensor where $\mu, \nu = \text{x}, \text{y}, \text{z}$ and $\delta_{\mu\nu}$ is a Kronecker delta such as

$$\text{A}_{\mu\nu}^{(A)} = \text{A}_{iso}^{(A)}\delta_{\mu\nu} + \text{A}_{\mu\nu}^{(A;dip)} + \text{A}_{\mu\nu}^{(A;SOC1)} + \text{A}_{\mu\nu}^{(A;SOC2)} \tag{2}$$

Since the isotropic contribution is based on the electronic spin density within the nucleus, transition metal atoms should not exhibit such contribution as the unpaired electron resides in *d* orbitals, which present a node at the nucleus position. However, the exchange terms for a d^1 system between the *d* orbital bearing the unpaired alpha electron and the paired core electrons differ for alpha and beta orbitals because such contributions are non-zero for electrons with the same spin. Thus, a spin-dependent interaction occurs within the atom, resulting in a spin polarisation of the inner shell *s* electrons. This exchange energy leads to a non-uniform distribution of the α and β electrons near the nucleus, consequently inducing a spin density in the internal orbitals.[30] Consequently, *s* orbitals, with their spherical symmetry, dominate the isotropic term in Equation 2 and require theoretical methods incorporating relativistic approaches to describe this term properly.[31] For a nucleus *A,* we use the following expression:

$$\text{A}_{iso}^{(A)} = \left(\frac{4}{3}\pi\langle S_z\rangle^{-1}\right) P^A \rho^{\alpha-\beta}(\mathbf{R}_A) \tag{3}$$

In this equation, $\langle S_z \rangle$ is the expectation value of the z-component of the total spin and $\rho^{\alpha-\beta}(\mathbf{R}_A)$ is the spin density at the centre of the nucleus, respectively. The proportionality constant is defined as:

$$P^A = \frac{\alpha}{2} g_e \mu_N g_N^{(A)} \tag{4}$$

Where $\alpha, \mu_N, g_N^{(A)}$ are the fine structure constant, nuclear magneton, and nuclear g-factor, respectively. The second term of Equation 2 is based on the classical dipole interaction between electronic and nuclear spins and is responsible for the dipolar contribution ($\mathbf{A}_{\mu\nu}^{(A;dip)}$). This term is expressed as the expectation value of the magnetic moment operator over the electron's spin density distribution for a nucleus *A* as:

$$\text{A}_{\mu\nu}^{(A;dip)} = \frac{1}{2S} P^A \sum_{p,q} P_{pq}^{\alpha-\beta} \left\langle \phi_p \left| r_A^{-5} \left(3\vec{r}_{A_\mu}\vec{r}_{A_\nu} - \delta_{\mu\nu} r_A^2\right) \right| \phi_q \right\rangle \tag{5}$$

Where $P_{pq}^{\alpha-\beta}$ is the spin-density matrix and $\vec{r}_A$ is the position vector of the electron relative to the nucleus ($\{\phi\}$ is the set of basis functions). Since the dipolar interaction exhibits dependence on r_A^{-3}, the integral can be simplified by retaining solely one-centre contributions. When introducing ligand-field theory, c_{Ai} relates to the covalency of the metal-ligand bonding and inclusion of the one-centre reduced field gradient integrals $f_{\mu\nu}$, states that dipole contributions are proportional to the expectation value of r_A^{-3} over the rather compact d-orbitals and the value P^A that can be substantial for some metal nuclei.[21]

$$\mathrm{A}_{\mu\nu}^{(A;dip)} = \frac{1}{2S} P_d \sum_i c_{Ai}^2 \langle d_i | f_{\mu\nu} | d_i \rangle \qquad (6)$$

$$P_d = P^A \langle r_A^{-3} \rangle_d \qquad (7)$$

The last two terms from Equation 2 are attributed to the spin-orbit coupling, which describes the second-order interaction between the electronic spin-magnetic moment and the orbit magnetic moment of the same and other electrons.

$$\begin{aligned}\mathrm{A}_{\mu\nu}^{(A;SOC1)} = \frac{1}{2S} P^A \Bigg\{ &\sum_{i(doubly)} \sum_{o_j(singly)} \Delta_{I_i^{o_j}}^{-1} \left\{ L_{3\mu}^{io_j} L_{1\nu}^{io_j} + L_{1\mu}^{io_j} L_{3\nu}^{io_j} \right\} \\ &- \sum_{o_i(singly)} \sum_{a(empty)} \Delta_{II_{o_i}^a}^{-1} \left\{ L_{3\mu}^{ao_j} L_{1\nu}^{ao_j} + L_{1\mu}^{ao_j} L_{3\nu}^{ao_j} \right\} \Bigg\} \qquad (8)\end{aligned}$$

where:

$$L_{1\mu}^{ij} = \mathrm{Im}\left(\langle \psi_i | \textstyle\sum_A \xi(r_A) l_\mu^A | \psi_j \rangle \right) \qquad (9)$$

$$L_{3\mu}^{ij} = \mathrm{Im}\left(\langle \psi_i | l_\mu^A r_A^{-3} | \psi_j \rangle \right) \qquad (10)$$

and:

$$\xi(r_{iA}) = \frac{\alpha^2}{2} \frac{Z_{eff}^A}{r_{iA}^3} \qquad (11)$$

The effective nuclear charges (Z_{eff}^A), used in the spin-orbit coupling expression are semi-empirical parameters. This expression considers two types of excitations: Type *I* involves an electronic promotion from a doubly occupied molecular orbital (*i*) to a singly occupied molecular orbital(o_j). Type *II*, on the other hand, entails a promotion from a singly occupied molecular orbital (o_i) to an empty orbital (*a*). Since only states with identical spin multiplicities contribute to the second-order HFC term, we restrict our focus to these states. This equation exhibits significant similarities to the expression for the second-order g-tensor ($g_{\mu\nu}$). This connection leads to:

$$\mathrm{A}_{\mu\nu}^{(A;SOC1)} = P_d \Delta g_{\mu\nu} \qquad (12)$$

The second spin-orbit coupling contribution comes from a cross-term between the electron-nuclear dipole-dipole Hamiltonian and the spin-orbit coupling. It is written as:

$$\begin{aligned}\mathrm{A}_{\mu\nu}^{(A;SOC2)} = -P^A \Bigg\{ &\sum_{i(doubly)} \Delta_{I_i^o}^{-1} \sum_{\kappa,\tau=x,y,z} \varepsilon_{\kappa\tau\mu} F_{\kappa\nu}^{io} L_{1\tau}^{io} \\ &- \sum_{a(empty)} \Delta_{II_o^a}^{-1} \sum_{\kappa,\tau=x,y,z} \varepsilon_{\kappa\tau\mu} F_{\kappa\nu}^{ao} L_{1\tau}^{ao} \Bigg\} \qquad (13)\end{aligned}$$

where:

$$F_{\mu\nu;\,A}^{ij} = \left(\langle \psi_i | r_A^{-5} \{ \delta_{\mu\nu} r_A^2 - 3 r_{A,\mu} r_{A,\nu} \} | \psi_j \rangle \right) \qquad (14)$$

Here, $\varepsilon_{\kappa\tau\mu}$ the Levi-Civitta symbol assumes a value of +1 for an even permutation and -1 for an odd permutation of κ, τ, μ. When considered within the ligand theory framework, using Eq. 13 we obtain:

$$\begin{aligned}\mathrm{A}_{\mu\nu}^{(A;SOC2)} &= -P_d \sum_i \sum_j \Delta_{ij}^{-1} (-1)^{\rho_{ij}} \zeta_{ij} c_{Mi}^2 c_{Mj}^2 \\ &\cdot \sum_{\kappa,\tau=x,y,z} i\varepsilon_{\kappa\tau\mu} \langle d_j | f_{\kappa\nu} | d_i \rangle \langle d_i | l_\tau^M | d_j \rangle \qquad (15)\end{aligned}$$

including the one-centre reduced field gradient integrals $f_{\mu\nu}$ and the angular momentum matrix elements between the d orbitals l_τ^M. The phase factor ρ_{ij} is zero if *i* is doubly occupied and unity if *i* is empty.

Computational Details

These effective Hamiltonian terms can be estimated using modern electronic structure methodologies. One relevant aspect for HFC calculation is a proper description of relativistic effects.[32, 33] Dirac's one-electron Hamiltonian containing a 4-spinor vector has been used as a four-component wavefunction. It describes the state of an electron, where these components are split as two-component spinor vectors. Even though the four-component methodology has remarkable accuracy as a potential candidate to describe quantum mechanical systems, it faces a heavy computational demand compared to Schrödinger-based methods.[34]

The major shortcoming surfaces from the positronic states (negative energy states) are coupled by the off-diagonal terms of Pauli's spin matrices.[35] As we are interested in electronic states, Hamiltonian corrections, which eliminate the negative energy components from the Dirac equation, presented very efficient results in practice, where zeroth-order regular approximation (ZORA)[36-39] stands out as a popular choice using a lower-order approximation. The exact decoupling of the upper and lower components of the spinor was achieved by Barysz and Sadlej,[40] leading to a unique transformation technique, the Douglas-Kroll-Hess (DKH) method.[41-43] Although presenting an interesting alternative to calculate fully relativistic quantum mechanics and properties, it also exhibits certain challenges, such as introducing spin-orbit and many-electron terms in the transformation of the many-electron Hamiltonian (in higher orders) and the calculation of molecular properties,[44] where picture change effects must be dealt with.[42] The eXact Two-Component (x2c) method offers an alternative to DKH for performing relativistic quantum chemistry calculations.[45-48] Unlike DKH, x2c utilises a non-iterative construction process. This means it directly obtains a matrix operator from the electronic solutions of the Fock-Roothaan equation. Additionally, x2c achieves a one-step solution by expanding the components of the 4-spinor in a one-electron basis set.[47] This bypasses the requirement for additional unitary transformations that contribute to the computational cost, as in DKH. As a result, x2c offers a streamlined approach that reduces computational effort compared to higher order DKH[35] which has been shown to yield notably accurate HFC and g-tensor calculations for a range of small 3d(1), 4d(1), and 5d(1) complexes, including larger 5d(7) Ir and Pt complexes.[49]

Basis and exchange-correlation functional assessment calculations were performed with Turbomole 7.7 package, using *ridft* module for x2c calculations, where the default density-fitted operator has been replaced by the exact operator.[50] All x2c calculations of EPR parameters were computed for three distinct orthogonal directions of the spin-magnetization.[51] A radial ultrafine/most dense grid (5a) was used for numerical quadrature. A 10^{-9} (Hartree) energy threshold was chosen unless stated otherwise. Computation of HFC-tensors was achieved using the x2c transformation applying the finite nucleus approximation.[52] The modified Scaled Nuclear Spin-Orbit (mSNSO) approximation was used to calculate HFC constants as suggested by Wodynski and Kaupp.[53] In troublesome cases, maximum and minimum damping settings were set to 1.5-0.5, and orbital shifting was added (0.2 eV). ZORA calculations were performed using the ORCA 5.0.4 package,[54, 55] employing B3LYP functional with an uncontracted version of ANO-DK3 basis set, adjusting to a 10^{-8} Hartree convergence criteria, and including picture change effects and finite nucleus approximation, unless stated otherwise. The hybrid functionals selected for benchmarking were B3LYP, [56] PBE0 [57] and a PBE40, as suggested by Wodynski and Kaupp for heavy metal complexes,[53] a PBE-based functional with 40% exact-type exchange. A long-range corrected functional was also analysed in the context of this study (ωB97X).[58] A series of basis sets, mainly relativistic, were experimented upon, including x2c-TZVPall,[50] x2c-TZVPPall,[50] x2c-QZVPPall,[59] x2c-QZVPPall-s,[59] def2-QZVPP,[60] UGBS,[61] ANO-DK3.[62] IGLO-III [63] was employed for light atoms in conjunction with ANO-DK3 and x2c-TZVPPall used for the metal.

The benchmark set of molecules comprised of a series of mononuclear first-row metal transition complexes showing large reported coherence times, consisting of $[Cu(mnt)_2]^{2-}$ (**1**),[22] $[V(dmit)_3]^{2-}$ (**2**),[19] $[V(C_8S_8)_3]^{2-}$ (**3**),[6] $[VO(dmit)_2]^{2-}$ (**4**),[19] and a Ti^{III} complex, [CpTi(cot)] (**5**).[64] For validation purposes we added Cu(Pc) (**6**),[65] $[V(C_6Br_4O_2)_3]^{2-}$ (**7**),[24] $[V(C_6H_4O_2)_3]^{2-}$ (**8**),[66] [Cu(acacen)] (**9**),[3] [Cu(tmtaa)] (**10**),[3] $[Cu(C_6H_4S_2)_2]^{2-}$ (**11**),[25] and $[Cu(C_6H_4Se_2)_2]^{2-}$ (**12**)[25]. The molecular structures determined by X-ray diffraction have been employed in the calculations (see Figure 1). However, it is important to keep in mind that experimentally, the EPR measurements for molecular qubits are carried out in frozen solution and magnetically diluted samples employing a non-magnetic metal cation that forms an isostructural complex (Further details regarding the computational implementation and its impact on the results can be found in Section 1 of the Supporting Information).

Additionally, model complexes with idealised symmetry have been generated using Shape 2.1 package[67, 68] employing V^{IV} as the main metal centre and NH_3 as ligands. The V-N bond distances were changed from the average of non-ideal DFT-optimized structures. The same code was employed to perform continuous shape measurements to determine the degree of distortion of the metal complexes in comparison with ideal coordination polyhedra.

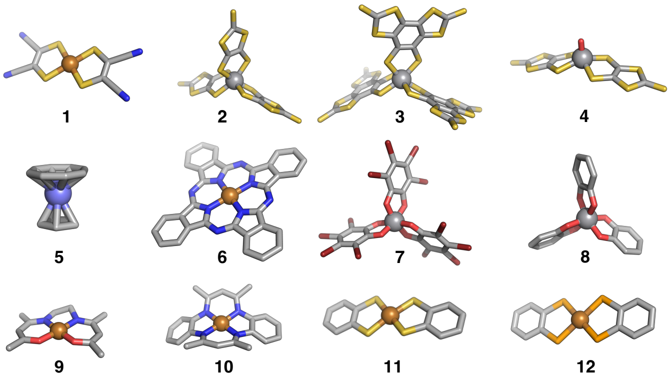

Figure 1. Molecular structure of the 12 studied qubit molecules. $[Cu(mnt)_2]^{2-}$ (**1**), $[V(dmit)_3]^{2-}$ (**2**), $[V(C_8S_8)_3]^{2-}$ (**3**), $[VO(dmit)_2]^{2-}$ (**4**), CpTi(cot) (**5**), Cu(Pc) (**6**), $[V(C_6Br_4O_2)_3]^{2-}$ (**7**), $[V(C_6H_4O_2)_3]^{2-}$ (**8**), [Cu(acacen)] (**9**), [Cu(tmtaa)] (**10**), $[Cu(C_6H_4S_2)_2]^{2-}$ (**11**) and $[Cu(C_6H_4Se_2)_2]^{2-}$ (**12**). Mnt = maleonitriledithiolate, dmit = 1,3-dithiole-2-thione-4,5-dithiolate, Cp = cyclopentadienyl, cot = 1,3,5,7-cyclooctatetraene, Pc = phthalocyanine, acacen = bis(acetylacetone)ethylenediamine, tmtaa = tetramethyltetraazaannulene. Hydrogens are hidden for clarity purposes. Orange, grey and purple spheres represent the metal atoms, copper, vanadium and titanium, respectively. Lighter elements are represented with sticks using grey, blue, red, yellow, and orange colours for carbon, nitrogen, oxygen, sulphur and selenium, respectively.

To quantify the accuracy in the prediction of A parameters, the Mean Absolute Percentage Logarithmic Error (MAPLE) was chosen as a metric for each approach according to:

$$MAPLE = \frac{1}{\mathrm{n}}\sum_{i=1}^{\mathrm{n}} \frac{\log\left|\mathrm{A}_i^{pred}\right| - \log\left|\mathrm{A}_i^{ref}\right|}{\log\left|\mathrm{A}_i^{ref}\right|} \qquad (16)$$

where A^{pred} and A^{ref} are the predicted and reference HFC constants, respectively, while n is the number of components. MAPLE benefits from a logarithmic transformation to reduce scale sensitivity in error measurements. By lowering the effect of larger values, it provides a more balanced error assessment than traditional metrics like MAE and MAPE, making it especially suitable for HFC constants with scale normalisation.

Results and Discussion

Benchmark Assessment for EPR Parameters Prediction

To evaluate the effect of the basis set and density functional in the calculation of HFC parameters, we selected a representative set of transition metal complexes proposed as molecular qubit candidates: $[V(dmit)_3]^{2-}$, $[Cu(mnt)_2]^{2-}$, $[V(C_8S_8)_3]^{2-}$, [CpTi(cot)] and $[VO(dmit)_2]^{2-}$ (compounds **1-5**). As illustrated in Figure 2, basis sets containing IGLO-III for lighter atoms in conjunction with ANO-DK3 and x2c-TZVPPall for the metal centre underperformed, proving inadequate for accurate HFC prediction in these systems. Triple-ξ basis sets yielded relatively high errors, between 25-28%, while quadruple-ξ basis sets performed significantly better with MAPLEs in the 10-14% range (excluding ωB97X results). A full basis set decontraction significantly improved predictions (e.g. ANO-DK3 MAPLE error reduced from 41% to 5% with the decontraction when used with B3LYP). To isolate the influence of a more detailed *s* orbital description on HFC constants, we modified the ANO-DK3 basis set by decontracting only the *s* functions. This reduced the error to 18%, suggesting that a more accurate description of higher angular momentum orbitals, even those not directly involved in bonding, can significantly impact HFC values. This observation aligns with Equation 3, indicating that a better description of the spin density $\rho^{\alpha-\beta}(\mathbf{R}_A)$ using heavier *s*-weighted function basis sets and adding *s*-primitives with large exponents improves the calculation of isotropic terms. NMR-shielded x2c-type basis sets (x2c-QZVPPall-s) were also evaluated but performed slightly worse than their non-shielded counterparts, showing approximately a 4% increase in MAPLE. For more numerically detailed results, check Tables S2-S6 in Supporting Information.

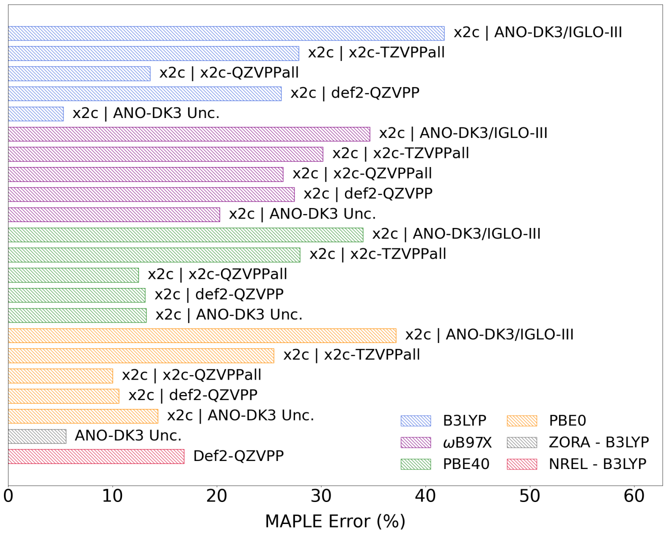

Figure 2. MAPLE error of computed HFC components employing various methodologies from compounds **1-5**. NREL stands for non-relativistic treatment. See Table S7 of the Supporting Information for the numerical details.

The evaluation of exchange-correlation functionals for HFC calculations revealed several notable trends. We focused our investigation on hybrid functionals based on previous research by Kossmann et al.[69], which demonstrated their superior performance over-generalized gradient approximation (GGA) functionals and highlighted their versatility across diverse compound classes compared to computationally more demanding double hybrid approaches. The impact of the functional choice demonstrated significantly less influential on HFC predictions compared to basis set selection. Nevertheless, when evaluating functionals with the best-performing basis set (uncontracted ANO-DK3), B3LYP emerged as the superior option with a remarkably low MAPLE of 5%, outperforming both PBE0 and PBE40, which showed MAPLEs of 14% and 13%, respectively. This finding differs somewhat from previous work by Kaupp and Wodyński,[53] where PBE40 showed excellent results for various transition metal complexes with the formula $[MOX_n]^{m-}$ (where M=Cr, Mo, Mn, Tc, Os, Re, W and X=F, Cl, Br) and larger Ir and Pt complexes. Surprisingly, the long-range separated hybrid functional ωB97X yielded the least average accurate results per functional among all tested functionals (Figure 2) and showed no significant improvement when changing basis sets. This functional failed to replicate HFC constants for several compounds accurately.

To evaluate the importance of relativistic effects in first-row transition metal complexes, we compared ZORA, x2c, and non-relativistic (NREL in Figure 2) treatments. ZORA demonstrated comparable accuracy to the x2c methodology, confirming its suitability for these systems. In contrast, non-relativistic calculations showed a MAPLE of 17%, highlighting the key influence of relativistic effects even for first-row transition metals. This suggests that the simplified ZORA approach may be preferable in some cases, offering a good balance between accuracy and computational efficiency. The impact of relativistic effects appeared less pronounced when dealing with lighter transition metal atoms compared to the effects of basis set choice and uncontracting. However, for systems containing heavier elements significantly affected by spin-orbit coupling, higher Hartree-Fock exchange might be beneficial to account for multiple two-electron terms and spin-other-orbit (2eSOO) contributions, which tend to dominate in such cases.[70-72]

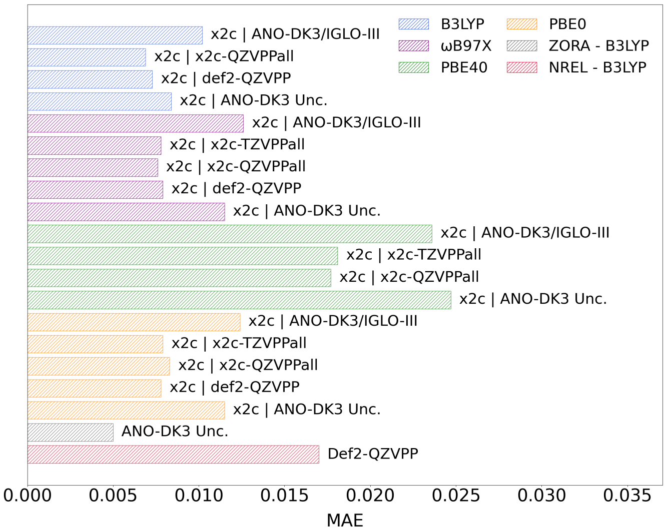

Figure 3. Average computed g-factor MAE error for compounds **1-5**. NREL stands for non-relativistic treatment. Numerical details are shown in Section 3 of Supporting Information.

In addition to HFC constants, g-values were also calculated for compounds **1-5**, which agree well with experimental reference values (see Figure 3 and Table S13). Regarding the choice of the density functional, B3LYP, ωB97X, and PBE0 performed similarly well, while PBE40 delivered significantly worse results. The basis set choice had a smaller impact, where we identified the contracted ANO-DK3/IGLO-III basis set as the one providing the highest error. ZORA, in conjunction with the uncontracted basis set, revealed to outperform every other methodology, proving superior in g-value prediction within these systems (See Tables S8-S12).

Based on these findings, we strongly recommend employing an uncontracted basis set, coupled with the B3LYP hybrid functional, demonstrating superior performance for these compounds. For relativistic treatment, ZORA provided an excellent balance between computational efficiency and accuracy, performing comparably to the x2c approach while reducing computational demands. To check how this computational procedure compares with experimental data, EPR parameters from best-performing methods were used to simulate continuous wave EPR (cw-EPR) and were compared against experimental EPR spectra for compound **2** in Figure 4. Experimental values reported in the literature were given as absolute magnitudes for most compounds as cw-EPR cannot determine the sign of HFC constants. To address this limitation, triple ENDOR (three-pulse) techniques[73, 74] enable the unambiguous sign assignment of HFC constants. However, almost no experimental sign measurements are reported due to the complexity of conducting such techniques. Simulations using EasySpin[75] were carried out to demonstrate no discernible impact of the HFC sign on EPR interpretation, as detailed in Section 4 of the Supporting Information. Compound **3** (Figure S3) raised significant discrepancies between the predicted and experimentally determined HFC constants, particularly for the perpendicular axes. This fact could be due to the fitting of the experimental EPR; it employed a single value for both perpendicular components.

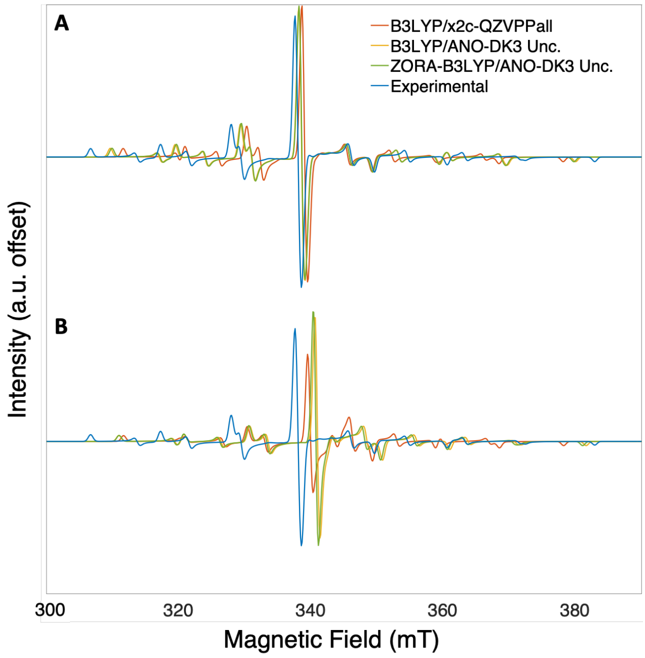

Figure 4. Simulated cw-EPR spectra of $[V(dmit)_3]^{2-}$ (**2**) using EasySpin version 6.0. **A.** Comparison between DFT computed and experimental hyperfine coupling constants setting experimental g-values. **B.** Comparison between computed and experimental EPR parameters. Simulated cw-EPR for the rest of the compounds can be found in Section 4 of Supporting Information.

An additional set of reported first-row transition metal molecular qubits consisting of [Cu(Pc)], $[V(C_6Br_4O_2)_3]^{2-}$, $[V(C_6H_4O_2)_3]^{2-}$, [Cu(acacen)], [Cu(tmtaa)], $[Cu(C_6H_4S_2)_2]^{2-}$ and $[Cu(C_6H_4Se_2)_2]^{2-}$ (compounds **6-12**) were selected to check how our computational proposal performed on a different set of molecules (Figure 5). For this second test, the B3LYP density functional was used with different choices of relativistic approximation (x2c and ZORA) and basis set (x2c-QZVPPall and ANO-DK3 uncontracted). EPR parameters for compounds **6-12** were also computed and gathered in Tables S13 and S14. Overall, ZORA managed to capture HFC arguably close to x2c results and exhibited superior accuracy for g-factor calculations. For compound **6**, the observed error primarily stemmed from overestimating the perpendicular HFC constants. Thus, we conclude that the ZORA approach remains accurate for the extended molecule set.

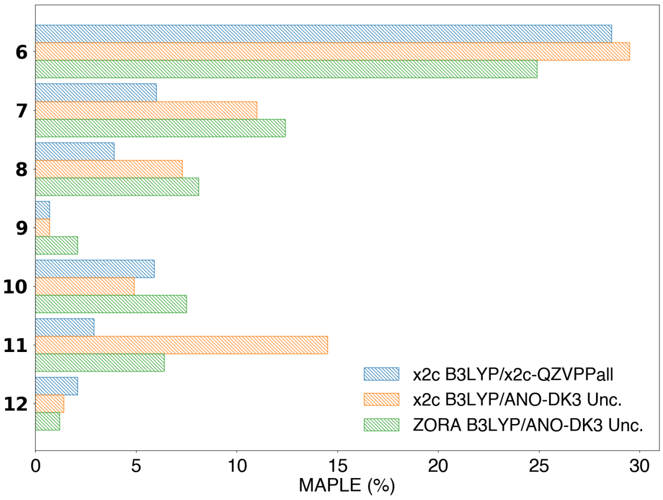

Figure 5. MAPLEs for computed HFC constants of compounds **6-12**. Numerical details can be found in Table S14.

Hyperfine Coupling Term Decomposition

While the isotropic term often dominates discussions due to its significant contribution in many systems, the spin-dipole and spin-orbit coupling terms can be of comparable magnitude under specific conditions. In systems with unpaired electrons primarily in *p* or *d* orbitals, the spin-dipole interaction becomes equally crucial. In molecules containing heavy atoms or those with significant orbital angular momentum, the spin-orbit coupling term, though sometimes overlooked, can contribute to hyperfine splitting of several MHz, particularly affecting g-tensor anisotropy, and zero-field splitting parameters.

The simultaneous effect of the three hyperfine coupling contributions necessitates a comprehensive approach to hyperfine engineering; any attempt to precisely control spin dynamics or interpret spectroscopic data must account for the modulation of all three hyperfine components. Neglecting any single term would result in significant quantitative and sometimes qualitative errors in predicting molecular behaviour. In this paper, we propose a decomposition of HFC for compounds **1-12**, enabling an in-depth evaluation of how structural changes in these systems correspond to shifts for the three contributions.

<u>Isotropic term:</u> the isotropic contribution (Fermi contact) is correlated to the spin density within the nucleus ($\rho^{\alpha-\beta}(\mathbf{R}_A)$ from Equation 3), where internal *1s*, *2s* and *3s* orbitals (inner shell) are the principal contributors.[76, 77] Orbitals *1s* and *2s* exhibit opposite spin density to that of the *3d* orbital,[78, 79] whereas orbital *3s* exhibited an opposite behaviour due to being closer to the *3d* orbital space, as revealed in Table S15. The *1s* orbital contributed minimally with β spin, suggesting negligible spin polarisation. Additionally, the *2s* orbital significantly contributed to the β spin density, as the spin polarisation from the Singly Occupied Molecular Orbital (SOMO) is significantly enhanced by the exchange interaction between these orbitals.[30] The *3s* orbital, due to its orthogonality to the *2s* orbital, overlaps with the *3d* metal orbital, and contributes to α spin. Markedly, the isotropic term also saw fluctuations not only from inner shell contributions but also from valence shell contributions. The latter phenomena resulted from formal ligand *p* orbitals creating two main interactions: with the metal centre inner shell, specifically *3s* orbital, forming molecular orbitals with antibonding character and another with the metal centre *3d* orbitals, forming a bonding molecular orbital where the corresponding non-bonding or anti-bonding molecular orbital becomes the SOMO. In both cases, these interactions share the same symmetry (A_1), making them permitted. The isotropic term for compounds **1-12** is depicted in Figure 6, split into inner (triangles), outer (squares), and total (circles) contributions. The results show a general trend with all compounds that there is a linear relationship between the Fermi contact and the nuclear spin density (see regression line in Fig. 6) according to Eq. 3. Overall, isotropic terms are negative except for the titanium compound (**5**, see Fig. S6), which exhibited a positive term due to the negative sign of its $g_N^{(A)}$ for the spin active nuclei (^{47}Ti and ^{49}Ti). Vanadium compounds (blues) showed a narrow isotropic term range of values, consisting of 5 compounds, from which 4 are octahedra, and one is a V$\mathrm{O^{II}}$ square pyramid. Inner contributions exhibited relatively constant values in a range between -0.2 and -0.3 $\mathrm{a.u.}^{-3}$. Positive valence contributions are found; oxygen atoms in the first coordination sphere had lower values, whereas sulphur ligands led to higher valence contributions. Copper systems (reds) exhibited higher isotropic terms in a broader range. All Cu$^{\mathrm{II}}$ complexes presented a square planar geometry for the first coordination sphere reflected by a consistent valence shell contribution (around -0.2 $\mathrm{a.u.}^{-3}$) as the coordination number remained the same. Inner shell contribution shifted to lower values as metal-ligand bond covalence increased, seeing how Cu-N and Cu-O exhibited the highest terms while Cu-S and Cu-Se showed the lowest inner contribution values not only for Cu$^{\mathrm{II}}$ but for the entire series of compounds. Covalence draws a trend on the inner contribution, reducing the strength of the isotropic term due to the delocalisation of spin density onto the ligands to which the metal is bonded. Interestingly, d^1 metal centres (V$^{\mathrm{IV}}$ and Ti$^{\mathrm{III}}$) showed a competitive tendency between contributions leading to overall lower magnitude isotropic terms, whereas d^9 metal centres (Cu$^{\mathrm{II}}$) exhibited higher isotropic magnitudes due to core and valence shell contributions enhancing each other.

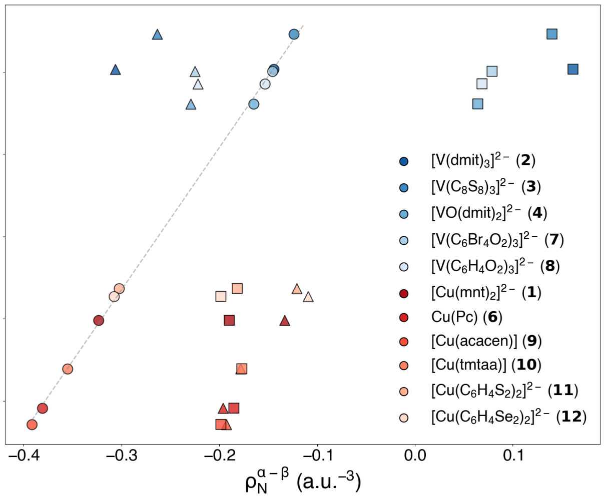

Figure 6. Correlation between isotropic term (Fermi contact) and nuclear spin density for compounds **1-12** (except compound **5**). Squares represent valence shell contributions, triangles represent core shell contributions and circles show the total contribution. Calculations were carried out employing B3LYP/ANO-DK3 and using ZORA relativistic treatment. Numerical details can be found in Table S15. For clarity purposes, to reduce the limits of the Fermi contact values, the Ti$^{\mathrm{III}}$ complex has not been included but can be checked in Figure S6.

<u>Spin-dipolar term:</u> Since the isotropic term is equal for all axes, the contribution responsible for the different shifts in HFC is attributed to the dipolar term. This can be related to the SOMO character, which is defined by the metal centre and its coordination environment. Equation 6 explains how, through the integration of the SOMO using the electric field gradient integrals, we can get a general trend for each system captured in Table S16.[21] Compound **1** presented a square planar geometry where the metal centre is a Cu$^{\mathrm{II}}$(d^9), and the SOMO is a $3d_{x^2-y^2}$. According to our evaluation, it showed a -2:1:1 relation between axes, which agreed with *ab initio* results.

Compounds **2** and **3** present pseudo-octahedral geometries with a V$^{\mathrm{IV}}$(d^1) and non-axial HFC components (see Tables S3-S4), which is likely a result of a symmetry-breaking shift induced by a Jahn-Teller distortion. We validated this theory via distortion analysis, which revealed that both compounds display a trigonal distortion, shifting from a regular octahedral (OC) geometry to a trigonal prism (TPR) as continuous shape measurement S(OC) values of 2.222 and 2.767 were obtained in contrast to S(TPR) values of 7.767 and 8.330. This distortion leads to a more stabilised d_{z^2} orbital and shifts the ratio in function of the degree of distortion. Further analysis shows that in compounds **2** and **3,** the SOMO is mostly a $3d_{yz}$ orbital, which should show a -2:1:1 spin-dipolar contributions according to Table S16. However, Jahn-Teller structural distortion in these compounds induces significant mixing of the d orbitals, departing from the expected trend. Compound **4** presented a square-base pyramid geometry with the metal out-of-plane and exhibited a similar trend as compound **1**, as its SOMO orbital is *3d*$_{xy}$, which shows in the same pattern than complex **1** SOMO (*3d*$_{x^2-y^2}$) (Table S16). This difference in SOMO between V^{IV} compounds, pseudo-octahedral **2** and **3** and vanadyl **4** complexes, explains the experimental and calculated values of the three HFC components (see Tables S3-S5), which are opposite between these two families of systems. The first ones present larger perpendicular HFC components, while the vanadyl axial component is the largest.

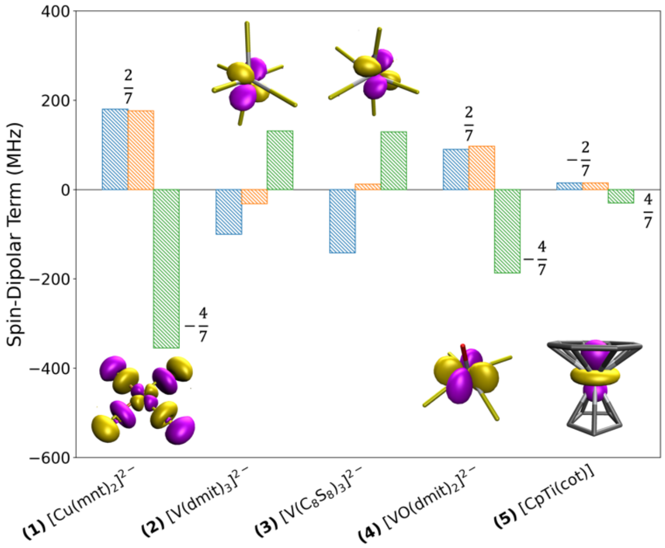

Figure 7. Spin-Dipolar term and SOMO visualisation for compounds **1-5**. Each colour bar represents an axis; blue, orange, and green display x, y and z, respectively. MOs were represented against the first coordination sphere. Compounds **2** and **3**, which present Jahn-Teller distortions, do not follow the axiality ratio in Table S16.

As mentioned earlier, compound **5** counts with a Ti^{III}(d^1) metal centre (which has a negative $g_N^{(A)}$) and an antiprism-like geometry, which portrayed a *3d*$_{z^2}$ SOMO, revealing an ideal relation in the spin-dipolar contributions, but with reversed signs. This leads to an almost vanishing contribution for this compound. Thus, we establish a clear relation between the pattern observed of the axial spin-dipolar terms and the nature of orbital bearing the unpaired electron, following the coefficients of the electric field gradient matrix elements (Table S16 and Eq. 6) for the systems without important mixing of d orbitals in the SOMO.

Spin-orbit term: The spin-orbit coupling contribution manifests through two distinct terms (as described in Equations 10 and 14), which, when summed, yield the total spin-orbit coupling contribution. The first term, as elaborated in the Hyperfine Coupling Contributions Section, directly depends on the g-factor shift (Eq. 12), while the second term originates from permitted excitations dictated by Hund's rule of multiplicity. The second spin-orbit coupling interaction is potentially smaller than the first since it depends on the energy gap between ground and excited states. Our comparison of $\Delta g_{\mu\nu}$ against $\mathrm{A}_{\mu\nu}^{SOC}$ (where $\mu = \nu$) for all experimental compounds presented in Figure 8, revealed a clear trend that supports the hypothesis of the first term dominating over the second ($\mathrm{A}_{\mu\nu}^{SOC1} \gg \mathrm{A}_{\mu\nu}^{SOC2}$). This way, $\mathrm{A}_{\mu\nu}^{SOC2}$ may be considered negligible (or constant), making $\mathrm{A}_{\mu\nu}^{SOC1}$ as the variable term that mostly controls the differences in the spin-orbit coupling contribution to the HFC. Thus, we can control the variation of this term by tuning the value of Δg.

Figure 8 shows compounds **1-12**, which fall into two distinct categories: d^1 complexes (containing V^{IV} and Ti^{III}) and d^9 complexes (containing Cu^{II}). Compounds with less than half-filled *d*-orbitals exhibited negative g-factor shifts and, consequently, negative spin-orbit coupling terms. In contrast, compounds with more than half-filled *d*-orbitals displayed positive g-shifts and positive spin-orbit coupling terms. Notably, Cu^{II} (d^9) compounds (**1**, **6**, **9-12**) exhibited positive g shifts, which lead to positive spin-orbit coupling contribution on all axes. Conversely, V^{IV} compounds (**2-4**, **7**, **8**) showed small negative g-shift values for every component and their $\mathbf{A}_{\mu\nu}^{SOC}$ values are either negative or small. As mentioned earlier, despite expecting negative spin-orbit coupling values for compound **5**, positive contributions were obtained due to having a negative g nuclear constant ($g_N^{(A)}$). The compounds in Figure 8 demonstrate how two of the three g-shift components are positioned much closer together, revealing a general axiality pattern. Our findings indicate that distortions, such as those exhibited by compounds **2** and **3**, disrupting this axiality. These distortions alter the spin-orbit coupling by changing the molecular anisotropy, resulting in more widely dispersed g values that reflect a more rhombic environment. Compounds **6** and **12** presented some deviation from the expected trend, possibly presenting a higher $\mathrm{A}_{\mu\nu}^{SOC2}$ value as opposed to the positive $\mathrm{A}_{\mu\nu}^{SOC1}$ term. Metal centres also dictated the magnitude of the spin-orbit coupling term, since changes to the nucleus impact on the $\xi(r_{iA})$ function (see Eq. 11), revealing higher spin-orbit coupling constants for heavier metals in Figure 8.

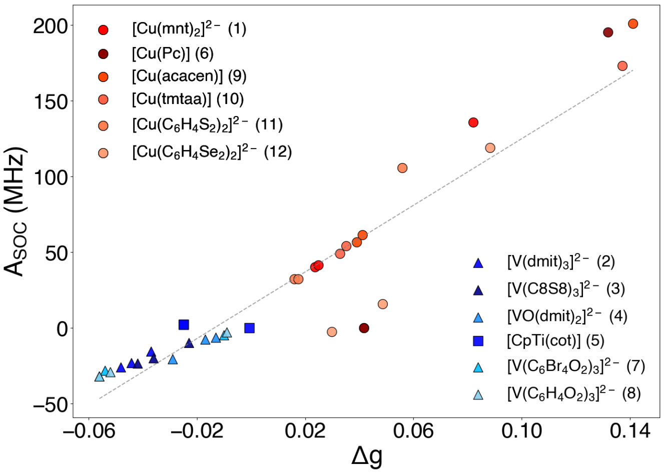

Figure 8. Computed $\Delta g_{\mu\nu}$ against total $\mathrm{A}_{\mu\nu}^{SOC}$ (where $\mu = \nu$) for compounds **1-12**. All calculations were performed using a fully uncontracted ANO-DK3 basis set and B3LYP employing a ZORA relativistic treatment.

Based on the detailed analysis of HFC components, we can propose a strategy for modulating HFC by targeting its three main contributions. Manipulation of the coordination environment and metal-ligand interactions are key. For the isotropic term, the choice of donor atoms can control the degree of covalency in metal-ligand bonds, affecting the s shell contributions due to the subtle balance between spin delocalisation and polarisation mechanisms. Modifying the symmetry of the coordination sphere through distortions (like Jahn-Teller effects) can significantly impact the spin-dipolar term by altering the SOMO character and the electric field gradient around the metal centre. For example, introducing trigonal distortions in octahedral complexes can break the orbital occupancy pattern from the ideal 1:1:-2 axial ratio. For the spin-orbit coupling contribution, selection of the metal centre is crucial, as heavier metals exhibit larger spin-orbit coupling constants. Additionally, the electron configuration of the metal (d^1 vs d^9) determines whether the g-shift and consequent spin-orbit coupling contribution will be negative or positive. Fine-tuning of the axiality or rhombicity in the three HFC parameters can be further modulated through the spin-orbit coupling term.

The Role of Metal Coordination on the Hyperfine Coupling

Variations in HFC depending on geometrical differences posed a question regarding the coordination environment and its implications. To explore this hypothesis further, we performed a computational study on V^{IV} homoleptic models coordinated with NH_3. The choice of nitrogen donor atoms instead of sulphur-based ligands as those analysed in the previous sections intends to avoid convergence problems due to highly negatively charged structures.

	A_{FC}	A_{SD}			A_{SOC}		
	A_{iso}	A_1	A_2	A_3	A_1	A_2	A_3
Trigonal Planar	-357	106	93	-200	-10	-83	-60
Vacant Tetrahedra	-225	96	110	-206	-10	-28	-70
Square Planar	-312	111	111	-223	47	47	-11
Tetrahedra	-90	-104	-104	209	-24	-24	-3
Seesaw	-174	108	101	-209	-32	-34	-24
Trigonal Bypiramid	-89	106	105	-210	-17	-76	-24
Square Based Pyramid	-109	104	104	-208	-24	-24	-19
Octahedra	-114	109	107	-216	-78	-82	-20
Trigonal Prism	-74	-112	-113	225	-20	-20	-3
Pentagonal Bypiramid	-126	116	86	-201	-8	-76	-24
Capped Ocathedra	-128	107	101	-208	-10	-24	-40

Figure 9. Heatmap of computed V^{IV} HFC components for $[V(NH_3)_x]^{4+}$ (where x = 3-7) geometric model complexes. All calculations were performed using B3LYP/ANO-DK3 approach and using ZORA relativistic treatment.

To visualize a general picture of computed HFC constants across the model structures, we generated a heatmap showing the magnitude and distribution of HFC constants for each geometric configuration (Figure 9). The highest Fermi contact terms were observed in trigonal planar, vacant tetrahedra, and square planar geometries. In low coordination systems (angular and linear), spin contamination aberrantly overestimated Fermi contact values, significantly degrading the accuracy of the results, which were discarded. While lower coordination geometries generally showed higher values, coordination number alone does not fully explain the trend, as evidenced by the low Fermi contact terms in trigonal bipyramidal and trigonal prismatic structures. Regardless, a common feature of the highest-yielding Fermi contact term compounds is their planar geometry. This term was further analysed in detail in Figure 10. Again, as we have previously seen in Fig. 6, there is a linear correlation between the isotropic contribution and the spin density in the metal nuclei centre. Inner-shell contributions comprise the sum of occupied core orbital (*1s*, *2s* and *3s*) contributions and consistently exhibited values found between -0.2 and -0.3 $a.u.^{-3}$ and remained relatively similar throughout all geometries, with no relevant trends observed. These valence shell effects can be predominantly attributed to the electronic contributions of the coordinating ligands. Notably, as metal-ligand distances increase, reduced molecular orbital overlap results in net positive contributions.[79] What is remarkable is that although this term is smaller than the contributions of the inner shells, it is, in fact, the one that makes the difference between the different modes of coordination as it is the only one that varies considerably from one system to another (see Fig. 10).

Analysis of the metal spin populations revealed values ranging from 1.08 to 1.31, with low-coordination compounds on the higher end. V^{IV} is a d^1 electronic configuration metal centre, and its SOMO has mainly non-bonding character, spin polarisation dominates over delocalisation, and there is no mixing with ligand orbitals. This α spin metal density could induce opposite spin density onto ligands, subsequently generating additional α spin density on the metal centre through a spin polarisation mechanism.

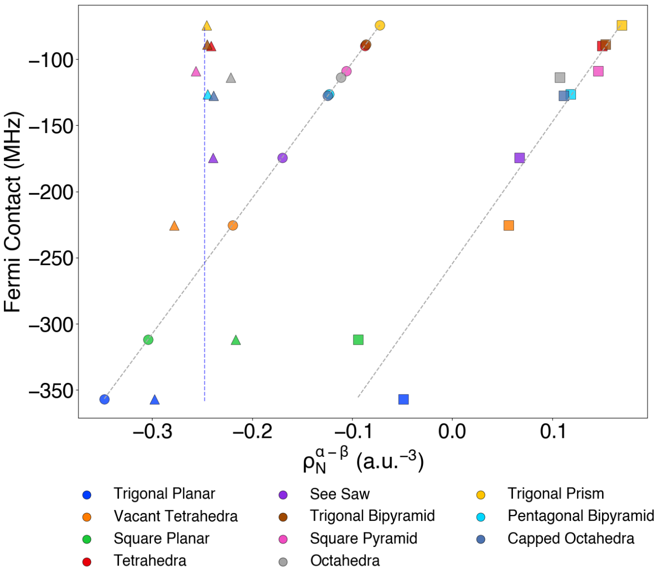

Figure 10. Correlation between Fermi contact contribution and total nuclear spin density for $[V(NH_3)_x]^{4+}$ (where x = 3-7) compounds. Squares, triangles, and circles represent the valence shell, core-shell and total contributions, respectively. Numerical details can be found in Table S17.

All systems showed relatively consistent spin-dipolar values, revealing axial ratios (1:1:2) between axis components in each system (as illustrated in Figure 9). Positive axial HFC values only were exhibited by the tetrahedra and trigonal prism compounds with a d_{z^2} SOMO, as expected from the one-centre reduced field integral values in Table S16. While Fermi contact interaction is isotropic, allowing only magnitude adjustments, the spin-dipolar interaction could selectively nullify one component while enhancing the others based on the SOMO configuration, which is determined by molecular geometry. Finally, the spin-orbit coupling component for all model compounds follows the same rule expressed in the previous section. The $A_{\mu\nu}^{SOC1}$ term seems to correlate directly with the Δg shift in a rather proportional manner (Figure S7). It could be assumed that this term dominates the changes in the spin-orbit coupling component, making the anisotropy the principal contributor. Overall, calculations on idealised $[V(NH_3)_x]^{4+}$ are consistent with the main factors determining the three terms for the hyperfine tensor identified for **1-12** real compounds. In addition, results on model systems provide new hints on how the coordination geometry can influence the Fermi contact term, as a lower coordination environment tends to enhance this contribution.

Conclusions

In the first part of this study employing DFT methods a benchmarking of hyperfine coupling has been performed using mononuclear transition metal complexes of the first series proposed as spin qubits. The best results are obtained by DFT methods employing the hybrid functional B3LYP together with methods including relativistic effects such as x2c or ZORA and quadruple-ζ or decontracted basis sets to provide a good description of the internal s orbitals. This methodology also provides good values for g, which can be considered predictive of the two essential quantities obtained from the continuous-wave EPR spectra. Larger discrepancies with the experimental values are obtained if other hybrid functionals such as PBE0 or ωB97X and basis sets of a lower quality are used.

The second part is devoted to a comprehensive analysis of HFC modulation in Cu^{II} and V^{IV} molecular spin qubits, examining the distinct contributions of Fermi contact, spin-dipolar, and spin-orbit-coupling terms across various coordination environments. Our results reveal that geometric configuration plays a critical role in determining HFC behaviour. This is evidenced by compounds **2**, **3** (pseudo-octahedral coordination) and **4** (vanadyl) which, despite sharing V^{IV} centres, exhibited markedly different HFC characteristics, non-axial and axial, respectively, due to their different coordination spheres and resulting SOMO orbitals.

We identified that pseudo-octahedral V^{IV} systems, as **2** and **3**, undergoing Jahn-Teller distortions serve as particularly promising candidates for spin qubit applications by breaking spin-Hamiltonian axiality. Systems with trigonal distortion demonstrate enhanced potential for orbital mixing with d_{z^2}, potentially leading to improved coherence properties. Our extended model analysis further revealed that trigonal planar, trigonal prismatic, and square planar configurations, where the z-axis remains relatively unperturbed by ligand interactions, offer favourable conditions for low-energy d_{z^2} orbitals to be the SOMO for d^1 configuration.

The HFC components exhibited distinctive patterns: Fermi contact contributions were predominantly negative, reflecting spin polarisation of inner-shell *s* electrons respect to the positive spin density of the SOMO. Their magnitude decreases in V^{IV} systems as coordination number increases due to nullifying effects from valence shell contributions. Spin-dipolar interactions displayed axial relation dependence on the SOMO, which could be disrupted through Jahn-Teller distortions. Spin-orbit coupling contributions showed direct correlation with Δg, with highly anisotropic molecules that could produce greater HFC shifts with more rhombic character. Based on these findings, we propose strategic approaches for HFC engineering in molecular spin qubits or quantum sensors. Previous work by Luis and colleagues demonstrated that achieving universal quantum operations requires hyperfine interactions that are neither purely axial nor purely isotropic, establishing specific relationships between the anisotropic parameters.[80] One promising strategy would involve enhancing the perpendicular HFC component while leveraging spin-dipolar contributions to differentiate the perpendicular axes. The metal centre can then be selected to fine-tune spin-orbit coupling effects through g-value modulation, with careful consideration of the anisotropy of the system. Alternatively, symmetry breaking via Jahn-Teller distortion offers a pathway to unequal spin-dipolar contributions, leading to rhombic systems where spin-orbit coupling further differentiates the three HFC components. These insights provide a foundation for the rational design of molecular spin qubits and quantum sensors with tailored HFC properties by understanding the interplay between geometric structure, electronic configuration, and the various contributions to HFC.

Author contributions

Joan Cardona: conceptualisation, methodology, formal analysis, investigation writing – original draft, review & editing. Àlex Solé:, conceptualization, investigation, writing – review & editing. Pablo Mella: conceptualisation, data curation. Daniel Aravena: conceptualisation, supervision, resources, validation, writing – review & editing. Javier Ruiz-Hidalgo: conceptualisation, supervision, resources, writing, funding acquisition – review & editing, funding acquisition. Silvia Gómez-Coca: conceptualisation, supervision, resources, writing – review & editing, funding acquisition. Eliseo Ruiz: conceptualisation, supervision, resources, writing – review & editing, funding acquisition.

Conflicts of interest

There are no conflicts to declare.

Data availability

The data supporting this article have been included as part of the Electronic Supplementary Information.

Acknowledgements

Financial support from Ministerio de Ciencia e Innovación (project PID2020-117142GB-I00, PID2021-122464NB-I00, TED2021-129593B-I00, CNS2023-144561 and Maria de Maeztu CEX2021-001202-M) is acknowledged. We also acknowledge the Generalitat de Catalunya for the 2021-SGR-00286 grant. E. R. also acknowledges the Generalitat de Catalunya for an ICREA Academia grant. We thank CSUC for the computational resources. P.M. thanks Universidad de Santiago de Chile, USACH, Project DICYT code 022242AP_Postdoc.

Notes and references

1. M. Atzori and R. Sessoli, The Second Quantum Revolution: Role and Challenges of Molecular Chemistry, *J. Am. Chem. Soc.*, 2019, **141**, 11339-11352.
2. E. Coronado, Molecular magnetism: from chemical design to spin control in molecules, materials and devices, *Nat. Rev. Mat.*, 2019, **5**, 87-104.
3. M. J. Amdur, K. R. Mullin, M. J. Waters, D. Puggioni, M. K. Wojnar, M. Gu, L. Sun, P. H. Oyala, J. M. Rondinelli and D. E. Freedman, Chemical control of spin–lattice relaxation to discover a room temperature molecular qubit, *Chem. Sci.*, 2022, **13**, 7034-7045.
4. J. M. Zadrozny, J. Niklas, O. G. Poluektov and D. E. Freedman, Millisecond Coherence Time in a Tunable Molecular Electronic Spin Qubit, *ACS Cent. Sci.*, 2015, **1**, 488-492.
5. E. Knill, R. Laflamme and G. J. Milburn, A scheme for efficient quantum computation with linear optics, *Nature*, 2001, 46–52.
6. C. J. Yu, M. J. Graham, J. M. Zadrozny, J. Niklas, M. D. Krzyaniak, M. R. Wasielewski, O. G. Poluektov and D. E. Freedman, Long Coherence Times in Nuclear Spin-Free Vanadyl Qubits, *J. Am. Chem. Soc.*, 2016, **138**, 14678-14685.
7. R. Blatt and D. Wineland, Entangled states of trapped atomic ions, *Nature*, 2008, **453**, 1008-1015.
8. P. D. Gregory, J. A. Blackmore, S. L. Bromley, J. M. Hutson and S. L. Cornish, Robust storage qubits in ultracold polar molecules, *Nat. Phys.*, 2021, **17**, 1149-1153.
9. J. Clarke and F. K. Wilhelm, Superconducting quantum bits, *Nature*, 2008, **453**, 1031-1042.
10. R. Hanson and D. D. Awschalom, Coherent manipulation of single spins in semiconductors, *Nature*, 2008, **453**, 1043-1049.
11. G. Aromí, D. Aguilà, P. Gamez, F. Luis and O. Roubeau, Design of magnetic coordination complexes for quantum computing, *Chem. Soc. Rev.*, 2012, **41**, 537-546.
12. L. Childress and R. Hanson, Diamond NV centers for quantum computing and quantum networks, *MRS Bull.*, 2013, **38**, 134-138.
13. Y. C. Liu, Y. C. Dzeng and C. C. Ting, Nitrogen Vacancy-Centered Diamond Qubit: The fabrication, design, and application in quantum computing, *IEEE Nanotechnol. Mag.*, 2022, **16**, 37-43.
14. D. P. DiVincenzo, The Physical Implementation of Quantum Computation, *Fortschr. Phys.*, 2000, **48**, 771-783.
15. A. Schweiger and G. Jeschke, *Principles of pulse electron paramagnetic resonance*, Oxford University Press, 2001.
16. M. S. Fataftah, M. D. Krzyaniak, B. Vlaisavljevich, M. R. Wasielewski, J. M. Zadrozny and D. E. Freedman, Metal-ligand covalency enables room temperature molecular qubit candidates, *Chem. Sci.*, 2019, **10**, 6707-6714.
17. A. M. Ariciu, D. H. Woen, D. N. Huh, L. E. Nodaraki, A. K. Kostopoulos, C. A. P. Goodwin, N. F. Chilton, E. J. L. McInnes, R. E. P. Winpenny, W. J. Evans and F. Tuna, Engineering electronic structure to prolong relaxation times in molecular qubits by minimising orbital angular momentum, *Nat. Commun.*, 2019, **10**, 3330.
18. D. Aravena and E. Ruiz, Spin dynamics in single-molecule magnets and molecular qubits, *Dalton Trans.*, 2020, **49**, 9916-9928.
19. M. Atzori, E. Morra, L. Tesi, A. Albino, M. Chiesa, L. Sorace and R. Sessoli, Quantum Coherence Times Enhancement in Vanadium(IV)-based Potential Molecular Qubits: the Key Role of the Vanadyl Moiety, *J. Am. Chem. Soc.*, 2016, **138**, 11234-11244.
20. A. Abragam and B. Bleaney, *Electron paramagnetic resonance of transition ions*, Oxford : Clarendon Press, 1970.
21. F. Neese and E. I. Solomon, in *Magnetism: Molecules to Materials IV*, 2002, ch. 9. Interpretation and Calculation of Spin-Hamiltonian Parameters in Transition Metal Complexes, pp. 345-466, WIley-VCH.
22. K. Bader, D. Dengler, S. Lenz, B. Endeward, S. D. Jiang, P. Neugebauer and J. van Slageren, Room temperature quantum coherence in a potential molecular qubit, *Nat. Commun.*, 2014, **5**, 5304.
23. S. Lenz, K. Bader, H. Bamberger and J. van Slageren, Quantitative prediction of nuclear-spin-diffusion-limited coherence times of molecular quantum bits based on copper(ii), *Chem. Comm.*, 2017, **53**, 4477-4480.
24. C. E. Jackson, C.-Y. Lin, S. H. Johnson, J. van Tol and J. M. Zadrozny, Nuclear-spin-pattern control of electron-spin dynamics in a series of V(iv) complexes, *Chem. Sci.*, 2019, **10**, 8447-8454.
25. M. S. Fataftah, M. D. Krzyaniak, B. Vlaisavljevich, M. R. Wasielewski, J. M. Zadrozny and D. E. Freedman, Metal–ligand covalency enables room temperature molecular qubit candidates, *Chem. Sci.*, 2019, **10**, 6707-6714.
26. M. J. Graham, M. D. Krzyaniak, M. R. Wasielewski and D. E. Freedman, Probing Nuclear Spin Effects on Electronic Spin Coherence via EPR Measurements of Vanadium(IV) Complexes, *Inorg. Chem.*, 2017, **56**, 8106-8113.
27. N. P. Kazmierczak, R. Mirzoyan and R. G. Hadt, The Impact of Ligand Field Symmetry on Molecular Qubit Coherence, *J. Am. Chem. Soc.*, 2021, **143**, 17305-17315.
28. M. Atzori, S. Benci, E. Morra, L. Tesi, M. Chiesa, R. Torre, L. Sorace and R. Sessoli, Structural Effects on the Spin Dynamics of Potential Molecular Qubits, *Inorg. Chem.*, 2018, **57**, 731-740.
29. K. R. Mullin, D. Johnson, D. E. Freedman and J. M. Rondinelli, Systems-chart approach to the design of spin relaxation times in molecular qubits, *Dalton Trans.*, 2024, **53**, 16585-16591.
30. M. L. Munzarová, P. Kubáček and M. Kaupp, Mechanisms of EPR Hyperfine Coupling in Transition Metal Complexes, *J. Am. Chem. Soc.*, 2000, **122**, 11900-11913.
31. K. G. Dyall, Interfacing relativistic and nonrelativistic methods. IV. One- and two-electron scalar approximations, *J. Chem. Phys.*, 2001, **115**, 9136-9143.
32. J. Autschbach, Relativistic Effects on Electron–Nucleus Hyperfine Coupling Studied with an Exact 2-Component (X2C) Hamiltonian, *J. Chem. Theory Comput.*, 2017, **13**, 710-718.

33. P. Verma and J. Autschbach, Relativistic Density Functional Calculations of Hyperfine Coupling with Variational versus Perturbational Treatment of Spin–Orbit Coupling, *J. Chem. Theory Comput.*, 2013, **9**, 1932-1948.
34. S. Gohr, P. Hrobárik, M. Repiský, S. Komorovský, K. Ruud and M. Kaupp, Four-Component Relativistic Density Functional Theory Calculations of EPR g- and Hyperfine-Coupling Tensors Using Hybrid Functionals: Validation on Transition-Metal Complexes with Large Tensor Anisotropies and Higher-Order Spin–Orbit Effects, *J. Phys. Chem. A.*, 2015, **119**, 12892-12905.
35. D. Peng and M. Reiher, Exact decoupling of the relativistic Fock operator, *Theor. Chem. Acc.*, 2012, **131**, 1081.
36. E. van Lenthe, E. J. Baerends and J. G. Snijders, Relativistic total energy using regular approximations, *J. Chem. Phys.*, 1994, **101**, 9783-9792.
37. E. van Lenthe, J. G. Snijders and E. J. Baerends, The zero-order regular approximation for relativistic effects: The effect of spin–orbit coupling in closed shell molecules, *J. Chem. Phys.*, 1996, **105**, 6505-6516.
38. E. v. Lenthe, E. J. Baerends and J. G. Snijders, Relativistic regular two-component Hamiltonians, *J. Chem. Phys.*, 1993, **99**, 4597-4610.
39. J. Autschbach and B. Pritchard, Calculation of molecular g-tensors using the zeroth-order regular approximation and density functional theory: expectation value versus linear response approaches, *Theor. Chem. Acc.*, 2011, **129**, 453-466.
40. M. Barysz and A. J. Sadlej, Infinite-order two-component theory for relativistic quantum chemistry, *J. Chem. Phys.*, 2002, **116**, 2696-2704.
41. B. Sandhoefer and F. Neese, One-electron contributions to the g-tensor for second-order Douglas–Kroll–Hess theory, *J. Chem. Phys.*, 2012, **137**, 094102.
42. M. Reiher, Douglas–Kroll–Hess Theory: a relativistic electrons-only theory for chemistry, *Theor. Chem. Acc.*, 2006, **116**, 241-252.
43. A. Wolf, M. Reiher and B. A. Hess, The generalized Douglas–Kroll transformation, *J. Chem. Phys.*, 2002, **117**, 9215-9226.
44. E. Malkin, I. Malkin, O. L. Malkina, V. G. Malkin and M. Kaupp, Scalar relativistic calculations of hyperfine coupling tensors using the Douglas–Kroll–Hess method with a finite-size nucleus model, *Phys. Chem. Chem. Phys.*, 2006, **8**, 4079-4085.
45. D. Peng and M. Reiher, Local relativistic exact decoupling, *J. Chem. Phys.*, 2012, **136**, 244108.
46. W. Kutzelnigg and W. Liu, Quasirelativistic theory equivalent to fully relativistic theory, *J. Chem. Phys.*, 2005, **123**, 241102.
47. Y. J. Franzke and J. M. Yu, Hyperfine Coupling Constants in Local Exact Two-Component Theory, *J. Chem. Theory Comput.*, 2022, **18**, 323-343.
48. S. Ghassemi Tabrizi, A. V. Arbuznikov, C. A. Jimenez-Hoyos and M. Kaupp, Hyperfine-Coupling Tensors from Projected Hartree-Fock Theory, *J. Chem. Theory Comput.*, 2020, **16**, 6222-6235.
49. Y. J. Franzke, F. Bruder, S. Gillhuber, C. Holzer and F. Weigend, Paramagnetic Nuclear Magnetic Resonance Shifts for Triplet Systems and Beyond with Modern Relativistic Density Functional Methods, *J. Phys. Chem. A*, 2024, **128**, 670-686.
50. P. Pollak and F. Weigend, Segmented Contracted Error-Consistent Basis Sets of Double- and Triple-zeta Valence Quality for One- and Two-Component Relativistic All-Electron Calculations, *J. Chem. Theory Comput.*, 2017, **13**, 3696-3705.
51. I. Malkin, O. L. Malkina, V. G. Malkin and M. Kaupp, Relativistic two-component calculations of electronic g-tensors that include spin polarization, *J. Chem. Phys.*, 2005, **123**, 244103.
52. L. Visscher and K. G. Dyall, Dirac–Fock Atomic Electronic Structure Calculations using Different Nuclear Charge Distributions, *At. Data Nucl. Data Tables*, 1997, **67**, 207-224.
53. A. Wodynski and M. Kaupp, Density Functional Calculations of Electron Paramagnetic Resonance g- and Hyperfine-Coupling Tensors Using the Exact Two-Component (X2C) Transformation and Efficient Approximations to the Two-Electron Spin-Orbit Terms, *J. Phys. Chem. A*, 2019, **123**, 5660-5672.
54. F. Neese, The ORCA program system, *Wiley Interdiscip. Rev. Comput. Mol. Sci.*, 2012, **2**, 73-78.
55. F. Neese, Software update: The ORCA program system—Version 5.0, *Wiley Interdiscip. Rev. Comput. Mol. Sci.*, 2022, **12**, e1606.
56. A. D. Becke, Density-functional thermochemistry. III. The role of exact exchange, *J. Chem. Phys.*, 1993, **98**, 5648-5652.
57. C. Adamo and V. Barone, Toward reliable density functional methods without adjustable parameters: The PBE0 model, *J. Chem. Phys.*, 1999, **110**, 6158-6170.
58. J.-D. Chai and M. Head-Gordon, Systematic optimization of long-range corrected hybrid density functionals, *J. Chem. Phys.*, 2008, **128**, 084106.
59. Y. J. Franzke, L. Spiske, P. Pollak and F. Weigend, Segmented Contracted Error-Consistent Basis Sets of Quadruple-ζ Valence Quality for One- and Two-Component Relativistic All-Electron Calculations, *J. Chem. Theory Comput.*, 2020, **16**, 5658-5674.
60. F. Weigend, F. Furche and R. Ahlrichs, Gaussian basis sets of quadruple zeta valence quality for atoms H–Kr, *J. Chem. Phys.*, 2003, **119**, 12753-12762.
61. E. V. R. de Castro and F. E. Jorge, Accurate universal Gaussian basis set for all atoms of the Periodic Table, *J. Chem. Phys.*, 1998, **108**, 5225-5229.
62. T. Tsuchiya, M. Abe, T. Nakajima and K. Hirao, Accurate relativistic Gaussian basis sets for H through Lr determined by atomic self-consistent field calculations with the third-order Douglas–Kroll approximation, *J. Chem. Phys.*, 2001, **115**, 4463-4472.
63. M. Schindler and W. Kutzelnigg, Theory of magnetic susceptibilities and NMR chemical shifts in terms of localized quantities. II. Application to some simple molecules, *J. Chem. Phys.*, 1982, **76**, 1919-1933.
64. L. C. de Camargo, M. Briganti, F. S. Santana, D. Stinghen, R. R. Ribeiro, G. G. Nunes, J. F. Soares, E. Salvadori, M. Chiesa, S. Benci, R. Torre, L. Sorace, F. Totti and R. Sessoli, Exploring the Organometallic Route to Molecular Spin Qubits: The [CpTi(cot)] Case, *Angew. Chem. Int. Ed.*, 2021, **60**, 2588-2593.
65. K. Bader, M. Winkler and J. van Slageren, Tuning of molecular qubits: very long coherence and spin–lattice relaxation times, *Chem. Comm.*, 2016, **52**, 3623-3626.
66. C.-Y. Lin, T. Ngendahimana, G. R. Eaton, S. S. Eaton and J. M. Zadrozny, Counterion influence on dynamic spin properties in a V(iv) complex, *Chem. Sci.*, 2019, **10**, 548-555.
67. D. Casanova, J. Cirera, M. Llunell, P. Alemany, D. Avnir and S. Alvarez, Minimal Distortion Pathways in Polyhedral Rearrangements, *J. Am. Chem. Soc.*, 2004, **126**, 1755-1763.
68. J. Cirera, E. Ruiz and S. Alvarez, Shape and Spin State in Four-Coordinate Transition-Metal Complexes: The Case of the d6 Configuration, *Chem. Eur. J.*, 2006, **12**, 3162-3167.
69. S. Kossmann, B. Kirchner and F. Neese, Performance of modern density functional theory for the prediction of hyperfine structure: meta-GGA and double hybrid functionals, *Mol. Phys.*, 2007, **105**, 2049-2071.
70. O. L. Malkina, B. Schimmelpfennig, M. Kaupp, B. A. Hess, P. Chandra, U. Wahlgren and V. G. Malkin, Spin–orbit corrections to NMR shielding constants from density functional theory. How

important are the two-electron terms?, *Chem. Phys. Lett.*, 1998, **296**, 93-104.

71. O. L. Malkina, J. Vaara, B. Schimmelpfennig, M. Munzarová, V. G. Malkin and M. Kaupp, Density Functional Calculations of Electronic g-Tensors Using Spin−Orbit Pseudopotentials and Mean-Field All-Electron Spin−Orbit Operators, *J. Am. Chem. Soc.*, 2000, **122**, 9206-9218.
72. J. Vaara, K. Ruud, O. Vahtras, H. Ågren and J. Jokisaari, Quadratic response calculations of the electronic spin-orbit contribution to nuclear shielding tensors, *J. Chem. Phys.*, 1998, **109**, 1212-1222.
73. D. Goldfarb and S. Stoll, *EPR Spectroscopy: Fundamentals and Methods*, 2018.
74. J. R. Harmer, in *eMagRes*, 2016, vol. 5, pp. 1493-1514.
75. S. Stoll and A. Schweiger, EasySpin, a comprehensive software package for spectral simulation and analysis in EPR, *J. Magn. Reson.*, 2006, **178**, 42-55.
76. E. Ruiz, J. Cirera and S. Alvarez, Spin density distribution in transition metal complexes, *Coord. Chem. Rev.*, 2005, **249**, 2649-2660.
77. A. Szabó and N. S. Ostlund, *Modern quantum chemistry : introduction to advanced electronic structure theory*, Mineola (N.Y.) : Dover publications, 1996.
78. R. J. Deeth, Discrete variational Xα calculations of the spectra of chlorocuprate(II) complexes: a detailed comparison with experiment and the cellular ligand field model, *Journal of the Chemical Society, Dalton Trans.*, 1990, 355-363.
79. J. Weber, A. Goursot, E. Penigault, J. H. Ammeter and J. Bachmann, Electronic structure of metallocene compounds. 3. Comparison of the results of multiple-scattering X.alpha. calculations with various electronic observables of cobaltocene, *J. Am. Chem. Soc.*, 1982, **104**, 1491-1506.
80. I. Gimeno, A. Urtizberea, J. Román-Roche, D. Zueco, A. Camón, P. J. Alonso, O. Roubeau and F. Luis, Broad-band spectroscopy of a vanadyl porphyrin: a model electronuclear spin qudit, *Chem. Sci.*, 2021, **12**, 5621-5630.

Supplementary Information (SI) for Chemical Science.

Supporting Information

Exploring Hyperfine Coupling in Molecular Qubits

Joan Cardona,[a] Àlex Solé,[a,b] Pablo Mella,[c] Daniel Aravena,[c] Javier Ruiz-Hidalgo,[b] Silvia Gómez-Coca[a] and Eliseo Ruiz[a]

---

[a] Departament de Química Inorgànica i Orgànica and Institut de Recerca de Química Teòrica i Computacional, Universitat de Barcelona, Diagonal 645, 08028 Barcelona, Spain.
[b] Department of Image Processing Group - Signal Theory and Communications Department, Universitat Politècnica de Catalunya, Jordi Girona 1-3, 08034 Barcelona, Spain.
[c] Departamento de Química de los Materiales, Facultad de Química y Biología, Universidad de Santiago de Chile, Casilla 40, Correo 33, Santiago, Chile.

Table of Contents

S1. Solvation Effects

EPR measurements can be performed using either a diamagnetic matrix or a frozen solution. When using a diamagnetic matrix, the central transition metal in the compound of interest is substituted with a diamagnetic element to create an isostructural complex. This approach eliminates contributions from the metal centre to the EPR spectrum. However, measurements in frozen solution are also possible. In such cases, careful consideration of external stimuli is crucial for reproducing experimental values. For instance. [CpTi(cot)] and $[V(C_8S_8)_3]^{2-}$ were measured in frozen solutions of toluene and CS_2, respectively. To achieve such effects, first an optimization of both structures was done using Gaussian 16, employing BP86/def2-TZVP and the Polarized Continuum Model (PCM). Then, HFC constants were calculated as indicated in the Computational Details section employing the Conductor-like Screening Model (COSMO). In conclusion, no significant changes were observed in the EPR spectra of the modified compounds. According to other compound references, diamagnetic matrices were prepared for compounds $[V(dmit)_3]^{2-}$, $[Cu(mnt)_2]^{2-}$ and $[VO(dmit)_2]^{2-}$ to conduct EPR measurements.

Table S1. HFC constants comparison between solvent-free, solvation model and experimental values.

Compound	Method	$A_\perp$ (MHz)	$A_\perp$ (MHz)	$A_\parallel$ (MHz)
$[V(C_8S_8)_3]^{2-}$	Solvent-free[a]	-294.7	-134.7	-5.7
	Solvation Model	-265.1	-158.1	25.7
	Experimental	**-258.0**	**-258.0**	**6.0**
[CpTi(cot)]	Solvent-free[a]	42.4	42.5	-5.8
	Solvation Model	40.8	40.8	-6.9
	Experimental	**52.4**	**52.4**	**ca. 5**

[a] Solvent-free approach calculation was performed using uncontracted ANO-DK3 basis set alongside B3LYP functional.

S2. Hyperfine Benchmark Assessment

Table S2. Computed hyperfine coupling constant values split into both perpendicular (⊥) and parallel (∥) components and the mean absolute percentage logarithmic error of $[Cu(mnt)_2]^{2-}$. Experimental values reported in the literature were given as absolute magnitudes.

Functional	Basis	$A_\perp$ (MHz)	$A_\perp$ (MHz)	$A_\parallel$ (MHz)	MAPLE (%)
B3LYP	ANO-DK3/IGLO-III	-20.3	-28.7	-305.5	24.8
	x2c-TZVPPall/IGLO-III	168.7	163.0	-251.7	8.4
	x2c-TZVPPall	165.9	160.2	-253.2	8.2
	x2c-TZVPall	162.1	156.6	-249.9	7.9
	x2c-QZVPPall	-103.3	-97.9	-504.0	2.3
	x2c-QZVPPall-s	-103.5	-98.0	-500.4	2.2
	def2-QZVPP	-42.6	-48.0	-464.7	13.8
	UGBS unc.	-80.3	-85.9	-495.8	5.0
	ANO-DK3 unc.	-85.7	-91.5	-497.9	4.0
	ANO-DK3 *s* unc.	-177.7	-189.8	-453.8	6.7
	ZORA – ANO-DK3 unc.	-80.1	-85.3	-520.4	5.2
	Non-relativistic – Def2-QZVPP	-87.2	-92.3	-537.7	4.2
ωB97X	ANO-DK3/IGLO-III	-63.9	-69.6	-390.6	9.3
	x2c-TZVPPall/IGLO-III	96.5	92.5	-367.1	4.8
	x2c-TZVPPall	93.6	89.6	-368.5	5.2
	x2c-QZVPPall	-183.0	-178.7	-627.7	7.2
	def2-QZVPP	-104.9	-108.8	-572.1	2.1
	ANO-DK3 Unc.	-161.0	-165.5	-611.7	5.6
PBE40	ANO-DK3/IGLO-III	-53.1	-59.3	-377.9	11.9
	x2c-TZVPPall/IGLO-III	212.4	207.7	-287.4	11.0
	x2c-TZVPPall	208.7	204.0	-289.7	10.7
	x2c-QZVPPall	-138.8	-143.6	-617.5	3.6
	def2-QZVPP	-61.3	-65.9	-564.5	9.3
	ANO-DK3 Unc.	-124.4	-129.1	-597.9	2.0
PBE0	ANO-DK3/IGLO-III	-34.0	-41.3	-331.2	18.2
	x2c-TZVPPall/IGLO-III	158.9	154.1	-283.2	7.0
	x2c-TZVPPall	155.6	150.8	-285.1	6.7
	x2c-QZVPPall	-134.4	-129.8	-555.6	2.1
	def2-QZVPP	-64.5	-69.0	-509.0	8.1
	ANO-DK3 Unc.	-114.5	-119.1	-544.6	0.7
Experimental		**118.0**	**118.0**	**500.0**	

Table S3. Computed hyperfine coupling constant values split into both perpendicular (⊥) and parallel (∥) components and the mean absolute percentage logarithmic error of $[\mathrm{V(dmit)_3}]^{2-}$. Experimental values reported in the literature were given as absolute magnitudes.

Functional	Basis	$A_{\perp}$ (MHz)	$A_{\perp}$ (MHz)	$A_{\parallel}$ (MHz)	MAPLE (%)
B3LYP	ANO-DK3/IGLO-III	227.4	67.9	-2.4	34.5
	x2c-TZVPPall/IGLO-III	236.9	54.0	-26.8	13.9
	x2c-TZVPPall	242.7	57.0	-24.7	14.1
	x2c-TZVPall	254.8	71.6	-8.7	21.9
	x2c-QZVPPall	-260.7	-182.2	-3.6	23.9
	x2c-QZVPPall-s	-257.4	-179.7	-2.9	26.2
	def2-QZVPP	-253.7	-169.8	20.6	8.8
	UGBS Unc.	-273.2	-200.1	-26.5	5.1
	ANO-DK3 Unc.	-275.9	-204.1	-31.9	3.3
	ANO-DK3 s Unc.	-311.1	-247.6	-93.8	8.4
	ZORA – ANO-DK3 Unc.	-273.8	-203.1	-32.4	3.2
	Non-relativistic – Def2-QZVPP	-269.7	-187.1	2.1	28.7
ωB97X	ANO-DK3/IGLO-III	262.6	79.8	5.0	26.0
	x2c-TZVPPall/IGLO-III	279.9	61.6	-27.7	11.8
	x2c-TZVPPall	287.3	66.3	-24.3	12.4
	x2c-QZVPPall	-220.2	-132.2	82.4	11.7
	def2-QZVPP	-221.4	-128.2	99.1	13.5
	ANO-DK3 Unc.	-240.5	-161.7	40.0	3.4
PBE40	ANO-DK3/IGLO-III	204.8	88.5	41.0	8.3
	x2c-TZVPPall/IGLO-III	236.9	54.0	-26.7	13.9
	x2c-TZVPPall	180.6	-72.1	6.0	27.2
	x2c-QZVPPall	-316.6	-242.3	-76.9	6.6
	def2-QZVPP	-305.5	-225.9	-48.4	2.0
	ANO-DK3 Unc.	-339.6	-279.4	-141.9	13.4
PBE0	ANO-DK3/IGLO-III	233.0	83.9	17.6	15.1
	x2c-TZVPPall/IGLO-III	187.4	-63.8	13.4	20.5
	x2c-TZVPPall	194.4	-60.9	17.4	18.2
	x2c-QZVPPall	-284.1	-209.2	-39.7	1.0
	def2-QZVPP	-273.8	-193.7	-12.5	12.1
	ANO-DK3 Unc.	-304.0	-236.1	-75.3	6.0
Experimental		**299.0**	**230.0**	**40.0**	

Table S4. Computed hyperfine coupling constant values split into both perpendicular (⊥) and parallel (∥) components and the mean absolute percentage logarithmic error of $[V(C_8S_8)_3]^{2-}$.

Functional	Basis	$A_\perp$ (MHz)	$A_\perp$ (MHz)	$A_\parallel$ (MHz)	MAPLE (%)
B3LYP	ANO-DK3/IGLO-III	216.0	93.6	-61.8	50.5
	x2c-TZVPPall/IGLO-III	225.6	94.2	-76.8	54.3
	x2c-TZVPPall	228.3	96.1	-75.7	53.8
	x2c-TZVPall	240.1	108.8	-60.3	48.5
	x2c-QZVPPall	-281.9	-116.2	10.7	16.1
	x2c-QZVPPall-s	-278.5	-114.5	11.0	16.6
	def2-QZVPP	-279.6	-102.6	33.0	37.7
	UGBS Unc.	-291.3	-132.8	-3.0	17.6
	ANO-DK3 Unc.	-294.7	-134.7	-5.7	5.5
	ANO-DK3 s Unc.	-323.8	-171.4	-48.4	42.6
	ZORA – ANO-DK3 Unc.	-292.2	-134.6	-6.8	7.0
	Non-relativistic – Def2-QZVPP	-292.8	-118.3	16.1	23.8
ωB97X	ANO-DK3/IGLO-III	247.5	107.8	-63.2	49.3
	x2c-TZVPPall/IGLO-III	260.5	109.0	-81.5	53.8
	x2c-TZVPPall	263.5	111.7	-79.6	53.3
	x2c-QZVPPall	-254.0	79.5	-67.3	52.1
	def2-QZVPP	-258.2	95.0	-60.6	49.0
	ANO-DK3 Unc.	-273.0	-96.1	51.3	46.2
PBE40	ANO-DK3/IGLO-III	227.8	106.8	-47.4	44.5
	x2c-TZVPPall/IGLO-III	190.2	-125.9	51.1	46.0
	x2c-TZVPPall	263.5	111.9	-79.8	53.3
	x2c-QZVPPall	-331.3	-158.3	-26.1	31.8
	def2-QZVPP	-327.7	-143.1	1.0	37.6
	ANO-DK3 Unc.	-347.7	-187.5	-56.3	45.4
PBE0	ANO-DK3/IGLO-III	224.0	103.0	-49.3	45.6
	x2c-TZVPPall/IGLO-III	186.1	-110.0	57.0	49.0
	x2c-TZVPPall	189.3	-108.2	59.6	49.8
	x2c-QZVPPall	-301.3	-140.1	-15.0	21.6
	def2-QZVPP	-296.4	-123.5	9.9	14.6
	ANO-DK3 Unc.	-316.8	-161.9	-36.6	37.7
Experimental		**-258.0**	**-258.0**	**6.0**	

Table S5. Computed hyperfine coupling constant values split into both perpendicular (⊥) and parallel (∥) components, and the mean absolute percentage logarithmic error of $[VO(dmit)_2]^{2-}$. Experimental values reported in the literature were given as absolute magnitudes.

Functional	Basis	$A_\perp$ (MHz)	$A_\perp$ (MHz)	$A_\parallel$ (MHz)	MAPLE (%)
B3LYP	ANO-DK3/IGLO-III	135.6	124.9	-163.3	5.4
	x2c-TZVPPall/IGLO-III	130.5	122.3	-180.4	5.3
	x2c-TZVPPall	132.5	124.6	-178.3	5.1
	x2c-TZVPall	147.0	139.1	-159.9	6.3
	x2c-QZVPPall	-77.4	-70.4	-369.5	8.6
	x2c-QZVPPall-s	-69.8	-76.5	-365.7	8.8
	def2-QZVPP	-53.4	-45.6	-363.2	14.2
	WTBS/UGBS Unc.	-81.9	-74.5	-376.3	7.8
	ANO-DK3 Unc.	-86.0	-78.2	-379.8	7.1
	ANO-DK3 s Unc.	-130.2	-118.3	-426.6	1.1
	ZORA – ANO-DK3 Unc.	-86.7	-79.0	-376.8	7.0
	Non-relativistic – Def2-QZVPP	-75.4	-68.0	-382.5	8.9
ωB97X	ANO-DK3/IGLO-III	136.5	126.8	-174.8	4.9
	x2c-TZVPPall/IGLO-III	138.2	129.9	-189.7	4.4
	x2c-TZVPPall	91.7	83.9	-214.2	9.3
	x2c-QZVPPall	-42.6	-35.1	-353.5	17.8
	def2-QZVPP	-23.1	-15.4	-349.9	27.6
	ANO-DK3 Unc.	-61.8	-54.5	-369.9	11.9
PBE40	ANO-DK3/IGLO-III	131.5	120.2	-179.2	5.4
	x2c-TZVPPall/IGLO-III	76.5	68.7	-246.3	11.1
	x2c-TZVPPall	78.7	71.2	-244.2	10.7
	x2c-QZVPPall	-131.8	-125.0	-434.8	0.8
	def2-QZVPP	-101.8	-94.1	-423.8	4.3
	ANO-DK3 Unc.	-145.6	-138.6	-446.3	1.3
PBE0	ANO-DK3/IGLO-III	138.3	126.9	-161.9	5.3
	x2c-TZVPPall/IGLO-III	89.7	81.7	-216.2	9.6
	x2c-TZVPPall	91.7	83.9	-214.2	9.3
	x2c-QZVPPall	-102.3	-95.3	-389.2	4.4
	def2-QZVPP	-75.8	-67.9	-380.8	8.9
	ANO-DK3 Unc.	-114.0	-106.5	-401.8	2.7
Experimental		**138.0**	**128.0**	**413.0**	

Table S6. Computed hyperfine coupling constant values split into both perpendicular ($\perp$) and parallel ($\parallel$) components, and the mean absolute percentage logarithmic error of [CpTi(cot)]. Experimental values reported in the literature were given as absolute magnitudes.

Functional	Basis	$A_{\perp}$ (MHz)	$A_{\perp}$ (MHz)	$A_{\parallel}$ (MHz)	MAPLE (%)
B3LYP	ANO-DK3/IGLO-III	-3.6	-3.5	-51.8	93.8
	x2c-TZVPPall/IGLO-III	16.0	16.1	-33.9	59.6
	x2c-TZVPPall	16.4	16.5	-32.3	58.1
	x2c-TZVPall	9.0	9.1	-40.3	72.8
	x2c-QZVPPall	39.2	39.3	-9.1	17.3
	x2c-QZVPPall-s	73.2	73.3	19.7	34.0
	def2-QZVPP	-13.1	38.0	38.1	56.4
	WTBS/UGBS Unc.	41.8	41.9	-6.4	8.9
	ANO-DK3 Unc.	42.4	42.5	-5.8	6.7
	ANO-DK3 s Unc.	47.4	47.2	-3.4	10.0
	ZORA – ANO-DK3 Unc.	42.0	42.1	-5.5	5.5
	Non-relativistic – Def2-QZVPP	40.6	40.7	-10.1	18.8
ωB97X	ANO-DK3/IGLO-III	-7.2	-7.1	-57.1	83.9
	x2c-TZVPPall/IGLO-III	9.8	9.9	-41.2	71.9
	x2c-TZVPPall	10.2	10.3	-40.5	70.9
	x2c-QZVPPall	26.9	27.1	-23.2	43.0
	def2-QZVPP	27.0	27.1	-25.6	45.0
	ANO-DK3 Unc.	31.7	31.8	-17.4	34.3
PBE40	ANO-DK3/IGLO-III	2.1	2.2	-46.8	100.0
	x2c-TZVPPall/IGLO-III	29.4	29.6	-20.7	39.1
	x2c-TZVPPall	29.9	30.1	-20.0	38.1
	x2c-QZVPPall	50.1	50.3	2.0	19.8
	def2-QZVPP	48.0	48.1	2.9	12.6
	ANO-DK3 Unc.	53.5	53.6	6.0	4.3
PBE0	ANO-DK3/IGLO-III	-2.1	-2.0	-49.4	101.8
	x2c-TZVPPall/IGLO-III	24.8	24.9	-23.4	44.5
	x2c-TZVPPall	25.4	25.4	-22.7	43.5
	x2c-QZVPPall	44.4	44.5	-2.1	21.1
	def2-QZVPP	42.7	42.8	-6.8	9.6
	ANO-DK3 Unc.	47.7	47.8	1.6	24.8
Experimental		**52.4**	**52.4**	**ca. 5**	

Table S7. Mean absolute percentile logarithmic error (MAPLE) for the methodologies shown in Figure 2.

Relativistic Treatment	Functional	Basis	MAPLE
x2c	B3LYP	ANO-DK3/IGLO-III	41.8
x2c	B3LYP	x2c –TZVPPall	27.9
x2c	B3LYP	x2c – QZVPPall	13.6
x2c	B3LYP	def2 – QZVPP	26.2
x2c	B3LYP	ANO – DK3 unc.	5.3
x2c	ωB97X	ANO-DK3|IGLO-III	34.7
x2c	ωB97X	x2c-TZVPPall|IGLO-III	29.3
x2c	ωB97X	x2c-TZVPPall	30.2
x2c	ωB97X	x2c-QZVPPall	26.4
x2c	ωB97X	def2-QZVPP	27.4
x2c	ωB97X	ANO-DK3 Unc.	20.3
x2c	PBE40	ANO-DK3|IGLO-III	34.0
x2c	PBE40	x2c-TZVPPall|IGLO-III	24.2
x2c	PBE40	x2c-TZVPPall	28.0
x2c	PBE40	x2c-QZVPPall	12.5
x2c	PBE40	def2-QZVPP	13.2
x2c	PBE40	ANO-DK3 Unc.	13.3
x2c	PBE0	ANO-DK3|IGLO-III	37.2
x2c	PBE0	x2c-TZVPPall|IGLO-III	26.1
x2c	PBE0	x2c-TZVPPall	25.5
x2c	PBE0	x2c-QZVPPall	10.0
x2c	PBE0	def2-QZVPP	10.7
x2c	PBE0	ANO-DK3 Unc.	14.4
ZORA	B3LYP	ANO-DK3U	5.5
Non-Rel.	B3LYP	Def2-QZVPP	16.9

S3. g-factor Benchmark Assessment

Table S8. Computed $[Cu(mnt)_2]^{2-}$ g-values and mean absolute error.

Functional	Basis	g_x	g_y	g_z	MAE
B3LYP	ANO-DK3/IGLO-III	2.0106	2.0207	2.0428	0.0213
	x2c-TZVPPall/IGLO-III	2.0202	2.0196	2.0717	0.0088
	x2c-TZVPPall	2.0201	2.0198	2.0719	0.0087
	x2c-TZVPall	2.0200	2.0198	2.0714	0.0089
	x2c-QZVPPall	2.0202	2.0198	2.0729	0.0083
	x2c-QZVPPall-s	2.0202	2.0198	2.0729	0.0083
	def2-QZVPP	2.0198	2.0203	2.0725	0.0084
	UGBS Unc.	2.0265	2.0254	2.0865	0.0042
	ANO-DK3 Unc.	2.0247	2.0236	2.0829	0.0042
	ANO-DK3 s Unc.	2.0126	2.0339	2.0557	0.0194
	ZORA – ANO-DK3 Unc.	2.0256	2.0273	2.0843	0.0052
ωB97X	ANO-DK3/IGLO-III	2.0133	2.0170	2.0532	0.0181
	x2c-TZVPPall/IGLO-III	2.0248	2.0233	2.0884	0.0023
	x2c-TZVPPall	2.0246	2.0229	2.0885	0.0020
	x2c-QZVPPall	2.0245	2.0232	2.0896	0.0017
	def2-QZVPP	2.0231	2.0248	2.0892	0.0019
	ANO-DK3 Unc.	2.0283	2.0304	2.1009	0.0072
PBE40	ANO-DK3/IGLO-III	2.0142	2.0175	2.0586	0.0159
	x2c-TZVPPall/IGLO-III	2.0339	2.0310	2.1220	0.0163
	x2c-TZVPPall	2.0337	2.0307	2.1219	0.0161
	x2c-QZVPPall	2.0340	2.0308	2.1229	0.0166
	def2-QZVPP	2.0310	2.0343	2.1240	0.0171
	ANO-DK3 Unc.	2.0365	2.0395	2.1356	0.0246
PBE0	ANO-DK3/IGLO-III	2.0117	2.0188	2.0464	0.0203
	x2c-TZVPPall/IGLO-III	2.0234	2.0215	2.0822	0.0041
	x2c-TZVPPall	2.0233	2.0216	2.0822	0.0040
	x2c-QZVPPall	2.0215	2.0233	2.0835	0.0036
	def2-QZVPP	2.0215	2.0237	2.0834	0.0038
	ANO-DK3 Unc.	2.0261	2.0285	2.0946	0.0038
Experimental		**2.0227**	**2.0227**	**2.0925**	

Table S9. Computed $[V(dmit)_3]^{2-}$ g-values and mean absolute error.

Functional	Basis	g_x	g_y	g_z	MAE
B3LYP	ANO-DK3/IGLO-III	1.9587	1.9628	1.9643	0.0104
	x2c-TZVPPall/IGLO-III	1.9610	1.9653	1.9672	0.0078
	x2c-TZVPPall	1.9606	1.9647	1.9672	0.0082
	x2c-TZVPall	1.9603	1.9644	1.9669	0.0085
	x2c-QZVPPall	1.9606	1.9671	1.9645	0.0083
	x2c-QZVPPall-s	1.9607	1.9647	1.9672	0.0081
	def2-QZVPP	1.9600	1.9641	1.9666	0.0088
	UGBS Unc.	1.9632	1.9529	1.9567	0.0162
	ANO-DK3 Unc.	1.9635	1.9528	1.9564	0.0164
	ANO-DK3 s Unc.	1.9396	1.9414	1.9529	0.0277
	ZORA – ANO-DK3 Unc.	1.9542	1.9581	1.9655	0.0131
ωB97X	ANO-DK3/IGLO-III	1.9449	1.9512	1.9569	0.0213
	x2c-TZVPPall/IGLO-III	1.9522	1.9584	1.9632	0.0144
	x2c-TZVPPall	1.9515	1.9579	1.9636	0.0147
	x2c-QZVPPall	1.9512	1.9578	1.9632	0.0149
	def2-QZVPP	1.9499	1.9569	1.9628	0.0158
	ANO-DK3 Unc.	1.9423	1.9503	1.9575	0.0223
PBE40	ANO-DK3/IGLO-III	1.8595	1.9252	1.9494	0.0610
	x2c-TZVPPall/IGLO-III	1.9611	1.9653	1.9673	0.0078
	x2c-TZVPPall	1.9152	1.9363	1.9454	0.0400
	x2c-QZVPPall	1.9144	1.9369	1.9465	0.0397
	def2-QZVPP	1.9124	1.9348	1.9447	0.0417
	ANO-DK3 Unc.	1.8897	1.9216	1.9397	0.0553
PBE0	ANO-DK3/IGLO-III	1.9481	1.9563	1.9594	0.0177
	x2c-TZVPPall/IGLO-III	1.9559	1.9603	1.9608	0.0133
	x2c-TZVPPall	1.9555	1.9601	1.9603	0.0137
	x2c-QZVPPall	1.9543	1.9589	1.9596	0.0147
	def2-QZVPP	1.9547	1.9593	1.9598	0.0144
	ANO-DK3 Unc.	1.9470	1.9554	1.9514	0.0211
Experimental		**1.9610**	**1.9710**	**1.9850**	

Table S10. Computed $[V(C_8S_8)_3]^{2-}$ g-values and mean absolute error.

Fuctional	Basis	g_x	g_y	g_z	MAE
B3LYP	ANO-DK3/IGLO-III	1.9783	1.9724	1.9669	0.013
	x2c-TZVPPall/IGLO-III	1.9810	1.9714	1.9672	0.012
	x2c-TZVPPall	1.9811	1.9713	1.9668	0.012
	x2c-TZVPall	1.9808	1.9710	1.9665	0.013
	x2c-QZVPPall	1.9811	1.9715	1.9668	0.012
	x2c-QZVPPall-s	1.9811	1.9714	1.9667	0.012
	def2-QZVPP	1.9808	1.9709	1.9661	0.013
	UGBS Unc.	1.9776	1.9660	1.9587	0.018
	ANO-DK3 Unc.	1.9785	1.9658	1.9596	0.017
	ANO-DK3 s Unc.	1.9718	1.9558	1.9483	0.027
	ZORA – ANO-DK3 Unc.	1.9602	1.9660	1.9798	0.022
ωB97X	ANO-DK3/IGLO-III	1.9748	1.9677	1.9560	0.019
	x2c-TZVPPall/IGLO-III	1.9803	1.9668	1.9580	0.017
	x2c-TZVPPall	1.9804	1.9667	1.9571	0.017
	x2c-QZVPPall	1.9803	1.9667	1.9571	0.017
	def2-QZVPP	1.9800	1.9658	1.9561	0.018
	ANO-DK3 Unc.	1.9773	1.9599	1.9476	0.024
PBE40	ANO-DK3/IGLO-III	1.9580	1.9497	1.9413	0.036
	x2c-TZVPPall/IGLO-III	1.9660	1.9593	1.9478	0.028
	x2c-TZVPPall	1.9804	1.9666	1.9576	0.017
	x2c-QZVPPall	1.9663	1.9594	1.9509	0.026
	def2-QZVPP	1.9653	1.9572	1.9460	0.029
	ANO-DK3 Unc.	1.9588	1.9508	1.9359	0.037
PBE0	ANO-DK3/IGLO-III	1.9724	1.9691	1.9615	0.018
	x2c-TZVPPall/IGLO-III	1.9772	1.9690	1.9636	0.015
	x2c-TZVPPall	1.9773	1.9691	1.9633	0.015
	x2c-QZVPPall	1.9769	1.9678	1.9613	0.017
	def2-QZVPP	1.9768	1.9685	1.9624	0.016
	ANO-DK3 Unc.	1.9744	1.9628	1.9550	0.021
Experimental		**1.9920**	**1.9920**	**1.9720**	

Table S11. Computed $[VO(dmit)_2]^{2-}$ g-values and mean absolute error.

Fuctional	Basis	g_x	g_y	g_z	MAE
B3LYP	ANO-DK3/IGLO-III	1.9855	1.9881	1.9787	0.0031
	x2c-TZVPPall/IGLO-III	1.9857	1.9879	1.9762	0.0022
	x2c-TZVPPall	1.9856	1.9880	1.9761	0.0022
	x2c-TZVPall	1.9855	1.9878	1.9759	0.0022
	x2c-QZVPPall	1.9855	1.9878	1.9762	0.0023
	x2c-QZVPPall-s	1.9855	1.9879	1.9763	0.0023
	def2-QZVPP	1.9877	1.9853	1.9759	0.0034
	WTBS/UGBS Unc.	1.9873	1.9838	1.9722	0.0026
	ANO-DK3 Unc.	1.9875	1.9838	1.9719	0.0015
	ANO-DK3 s Unc.	1.9830	1.9884	1.9653	0.0027
	ZORA – ANO-DK3 Unc.	1.9890	1.9857	1.9734	0.0020
ωB97X	ANO-DK3/IGLO-III	1.9844	1.9865	1.9742	0.0024
	x2c-TZVPPall/IGLO-III	1.9846	1.9864	1.9716	0.0015
	x2c-TZVPPall	1.9845	1.9869	1.9744	0.0023
	x2c-QZVPPall	1.9844	1.9863	1.9716	0.0016
	def2-QZVPP	1.9861	1.9842	1.9712	0.0017
	ANO-DK3 Unc.	1.9857	1.9829	1.9671	0.0028
PBE40	ANO-DK3/IGLO-III	1.9801	1.9826	1.9719	0.0044
	x2c-TZVPPall/IGLO-III	1.9832	1.9811	1.9686	0.0037
	x2c-TZVPPall	1.9811	1.9833	1.9686	0.0037
	x2c-QZVPPall	1.9811	1.9833	1.9692	0.0035
	def2-QZVPP	1.9804	1.9826	1.9684	0.0042
	ANO-DK3 Unc.	1.9784	1.9818	1.9641	0.0066
PBE0	ANO-DK3/IGLO-III	1.9842	1.9869	1.9768	0.0032
	x2c-TZVPPall/IGLO-III	1.9845	1.9868	1.9745	0.0024
	x2c-TZVPPall	1.9845	1.9869	1.9744	0.0023
	x2c-QZVPPall	1.9844	1.9868	1.9746	0.0025
	def2-QZVPP	1.9841	1.9865	1.9742	0.0025
	ANO-DK3 Unc.	1.9826	1.9862	1.9701	0.0018
Experimental		**1.9860**	**1.9880**	**1.9700**	

Table S12. Computed [CpTi(cot)] g-values and mean absolute error.

Fuctional	Basis	g_x	g_y	g_z	MAE
B3LYP	ANO-DK3/IGLO-III	1.9765	1.9771	2.0004	0.0034
	x2c-TZVPPall/IGLO-III	1.9770	1.9773	2.0004	0.0036
	x2c-TZVPPall	1.9770	1.9775	2.0004	0.0037
	x2c-TZVPall	1.9768	1.9773	2.0004	0.0036
	x2c-QZVPPall	1.9768	1.9772	2.0003	0.0036
	x2c-QZVPPall-s	1.9647	1.9652	2.0005	0.0049
	def2-QZVPP	1.9764	1.9769	2.0003	0.0033
	WTBS/UGBS Unc.	1.9749	1.9754	2.0002	0.0024
	ANO-DK3 Unc.	1.9750	1.9756	2.0001	0.0025
	ANO-DK3 s Unc.	1.9658	1.9665	1.9997	0.0043
	ZORA – ANO-DK3 Unc.	1.9769	1.9773	2.0016	0.0036
ωB97X	ANO-DK3/IGLO-III	1.9746	1.9749	2.0003	0.0021
	x2c-TZVPPall/IGLO-III	1.9756	1.9759	2.0004	0.0027
	x2c-TZVPPall	1.9752	1.9758	2.0004	0.0025
	x2c-QZVPPall	1.9748	1.9752	2.0004	0.0022
	def2-QZVPP	1.9743	1.9747	2.0004	0.0019
	ANO-DK3 Unc.	1.9732	1.9737	2.0001	0.0013
PBE40	ANO-DK3/IGLO-III	1.9728	1.9733	2.0003	0.0009
	x2c-TZVPPall/IGLO-III	1.9745	1.9746	2.0005	0.0019
	x2c-TZVPPall	1.9744	1.9746	2.0004	0.0019
	x2c-QZVPPall	1.9751	1.9750	2.0003	0.0023
	def2-QZVPP	1.9735	1.9742	2.0004	0.0014
	ANO-DK3 Unc.	1.9713	1.9726	2.0000	0.0008
PBE0	ANO-DK3/IGLO-III	1.9768	1.9772	2.0004	0.0035
	x2c-TZVPPall/IGLO-III	1.9769	1.9779	2.0005	0.0038
	x2c-TZVPPall	1.9768	1.9776	2.0004	0.0037
	x2c-QZVPPall	1.9772	1.9780	2.0003	0.0040
	def2-QZVPP	1.9764	1.9769	2.0004	0.0033
	ANO-DK3 Unc.	1.9760	1.9762	2.0001	0.0030
Experimental		**1.9720**	**1.9720**	**2.0010**	

Table S13. Computed g-values and mean absolute error for compounds **6 – 12**.

Compound	Method	g_x	g_y	g_z	MAE
[Cu(Pc)]	x2c – B3LYP / x2c-QZVPPall	2.0378	2.0378	2.1254	0.0324
	x2c – B3LYP / ANO-DK3 Unc.	2.0416	2.0416	2.1333	0.0272
	ZORA – B3LYP / ANO-DK3 Unc.	2.0439	2.0440	2.1342	0.0254
	Experimental	**2.0496**	**2.0496**	**2.1990**	
$[V(C_6Br_4O_2)_3]^{2-}$	x2c – B3LYP / x2c-QZVPPall	1.9514	1.9491	1.9912	0.0142
	x2c – B3LYP / ANO-DK3 Unc.	1.9479	1.9451	1.9905	0.0115
	ZORA – B3LYP / ANO-DK3 Unc.	1.9465	1.9485	1.9925	0.0128
	Experimental	**1.9380**	**1.9210**	**1.9900**	
$[V(C_6H_4O_2)_3]^{2-}$	x2c – B3LYP / x2c-QZVPPall	1.9534	1.9491	1.9913	0.0109
	x2c – B3LYP / ANO-DK3 Unc.	1.9469	1.9421	1.9905	0.0065
	ZORA – B3LYP / ANO-DK3 Unc.	1.9505	1.9459	1.9936	0.0097
	Experimental	**1.9420**	**1.9280**	**1.9910**	
[Cu(acacen)]	x2c – B3LYP / x2c-QZVPPall	2.0345	2.0375	2.1346	0.0211
	x2c – B3LYP / ANO-DK3 Unc.	2.0384	2.0405	2.1426	0.0162
	ZORA – B3LYP / ANO-DK3 Unc.	2.0414	2.0434	2.1435	0.0139
	Experimental	**2.0450**	**2.0450**	**2.1800**	
[Cu(tmtaa)]	x2c – B3LYP / x2c-QZVPPall	2.0327	2.0285	2.1335	0.0192
	x2c – B3LYP / ANO-DK3 Unc.	2.0353	2.0327	2.1392	0.0196
	ZORA – B3LYP / ANO-DK3 Unc.	2.0351	2.0375	2.1395	0.0210
	Experimental	**2.0250**	**2.0250**	**2.1800**	
$[Cu(C_6H_4S_2)_2]^{2-}$	x2c – B3LYP / x2c-QZVPPall	2.0123	2.0135	2.0443	0.0176
	x2c – B3LYP / ANO-DK3 Unc.	2.0133	2.0134	2.0358	0.0202
	ZORA – B3LYP / ANO-DK3 Unc.	2.0183	2.0198	2.0581	0.0095
	Experimental	**2.0190**	**2.0190**	**2.0850**	
$[Cu(C_6H_4Se_2)_2]^{2-}$	x2c – B3LYP / x2c-QZVPPall	2.0229	2.0452	2.0885	0.0129
	x2c – B3LYP / ANO-DK3 Unc.	2.0218	2.0475	2.0850	0.0121
	ZORA – B3LYP / ANO-DK3 Unc.	2.0322	2.0509	2.0906	0.0186
	Experimental	**2.0180**	**2.0180**	**2.0820**	

Table S14. Computed and experimental HFC constants of compounds **6–12**. Experimental values reported in the literature were given as absolute magnitudes.

Compound	Method	$A_\perp$ (MHz)	$A_\perp$ (MHz)	$A_\parallel$ (MHz)	MAPLE (%)
[Cu(Pc)]	x2c – B3LYP / x2c-QZVPPall	-47.6	-48.1	-634.8	28.6
	x2c – B3LYP / ANO-DK3 Unc.	-49.5	-50.0	-633.4	29.5
	ZORA – B3LYP / ANO-DK3 Unc.	-40.5	-41.0	-666.6	24.9
	Experimental	**15.0**	**15.0**	**630.0**	
$[V(C_6Br_4O_2)_3]^{2-}$	x2c – B3LYP / x2c-QZVPPall	-188.7	-331.1	40.9	6.0
	x2c – B3LYP / ANO-DK3 Unc.	-195.7	-340.2	21.2	11.0
	ZORA – B3LYP / ANO-DK3 Unc.	-195.4	-335.8	18.0	12.4
	Experimental	**280.0**	**365.0**	**60.0**	
$[V(C_6H_4O_2)_3]^{2-}$	x2c – B3LYP / x2c-QZVPPall	-246.1	-304.8	49.7	3.9
	x2c – B3LYP / ANO-DK3 Unc.	-255.5	-316.0	31.4	7.3
	ZORA – B3LYP / ANO-DK3 Unc.	-253.4	-310.9	28.7	8.1
	Experimental	**310.0**	**367.0**	**60.0**	
[Cu(acacen)]	x2c – B3LYP / x2c-QZVPPall	-59.9	-64.4	-634.2	0.7
	x2c – B3LYP / ANO-DK3 Unc.	-62.1	-66.6	-630.1	0.7
	ZORA – B3LYP / ANO-DK3 Unc.	-54.1	-57.1	-662.5	2.1
	Experimental	**63.0**	**63.0**	**650.0**	
[Cu(tmtaa)]	x2c – B3LYP / x2c-QZVPPall	-46.4	-43.2	-606.2	5.9
	x2c – B3LYP / ANO-DK3 Unc.	-49.5	-45.5	-605.9	4.9
	ZORA – B3LYP / ANO-DK3 Unc.	-38.8	-41.0	-635.0	7.5
	Experimental	**65.0**	**65.0**	**620.0**	
$[Cu(C_6H_4S_2)_2]^{2-}$	x2c – B3LYP / x2c-QZVPPall	-91.3	-95.9	-504.7	2.9
	x2c – B3LYP / ANO-DK3 Unc.	-45.5	-42.3	-421.6	14.5
	ZORA – B3LYP / ANO-DK3 Unc.	-72.3	-77.0	-525.0	6.4
	Experimental	**115.0**	**115.0**	**500.0**	
$[Cu(C_6H_4Se_2)_2]^{2-}$	x2c – B3LYP / x2c-QZVPPall	-136.9	-114.0	-453.0	2.1
	x2c – B3LYP / ANO-DK3 Unc.	-147.4	-121.5	-452.2	1.4
	ZORA – B3LYP / ANO-DK3 Unc.	-123.0	-143.6	-461.1	1.2
	Experimental	**145.0**	**145.0**	**460.0**	

S4. EPR Simulations

In our computational analysis, the magnitudes of the hyperfine coupling constants were found to be sufficient for interpreting the observed splitting. The signs of the HFC constants, however, were not determinative. Reversing the signs of the experimental coupling constants resulted in equivalent spectra, with no observable change as seen in Figure S1.

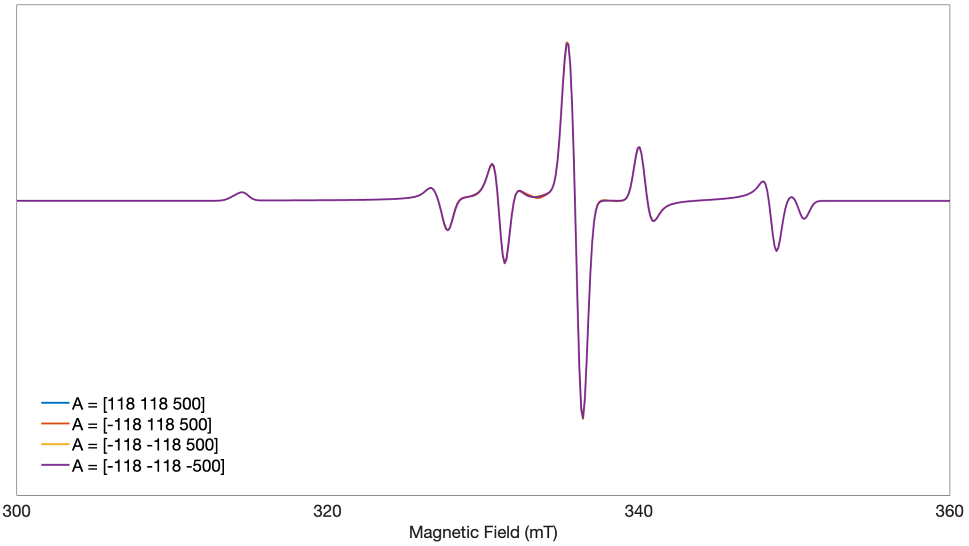

Figure S1. $[Cu(mnt)_2]^{2-}$ computed cw-EPR spectra using experimental EPR parameter values showing no differences upon sign reversal of one and multiple HFC components.

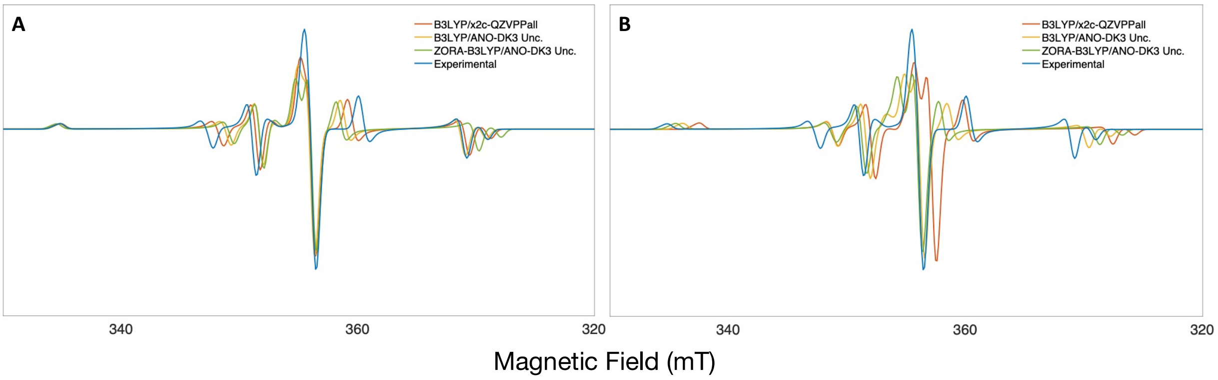

Figure S2. Simulated cw-EPR spectra of $[Cu(mnt)_2]^{2-}$ using EasySpin version 6.0. **A.** Comparison between computed and experimental hyperfine coupling constants setting experimental g-values. **B.** Comparison between computed and experimental EPR parameters.

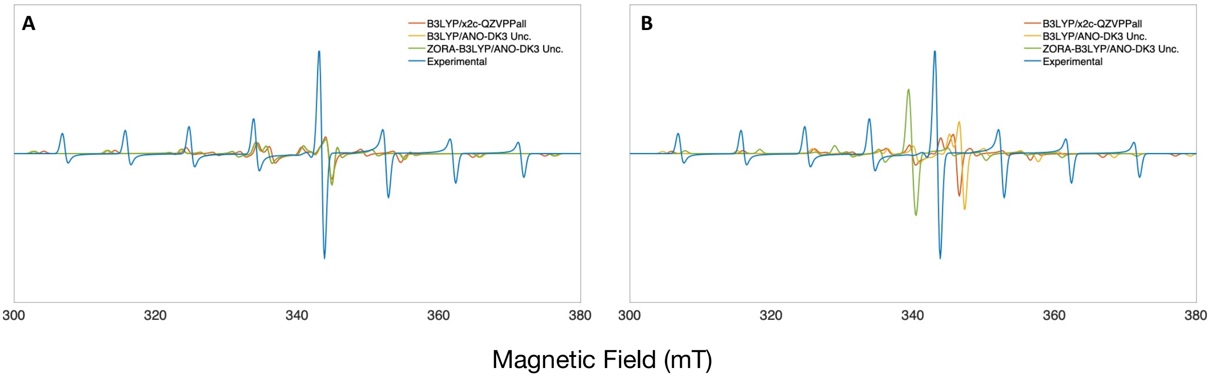

Figure S3. Simulated cw-EPR spectra of $[V(C_8S_8)_3]^{2-}$ using EasySpin version 6.0. **A.** Comparison between computed and experimental hyperfine coupling constants setting experimental g-values. **B.** Comparison between computed and experimental EPR parameters.

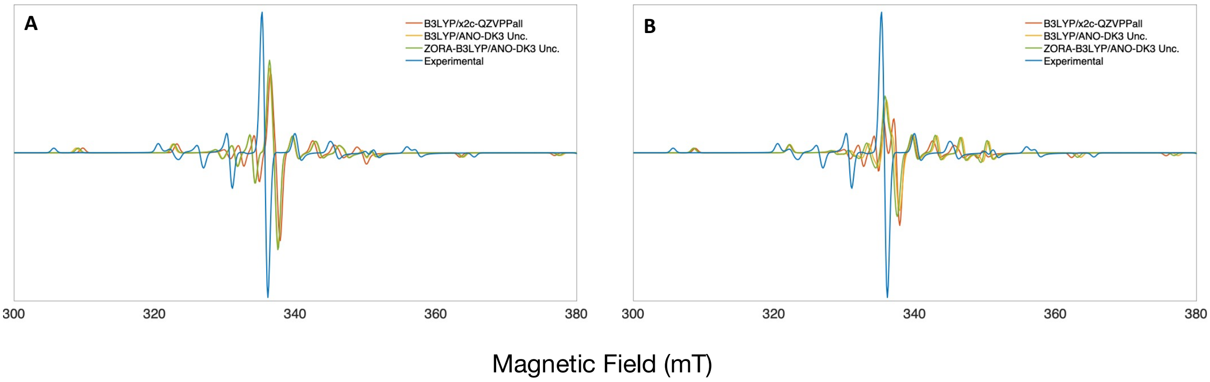

Figure S4. Simulated cw-EPR spectra of $[VO(dmit)_2]^{2-}$ using EasySpin version 6.0. **A.** Comparison between computed and experimental hyperfine coupling constants setting experimental g-values. **B.** Comparison between computed and experimental EPR parameters.

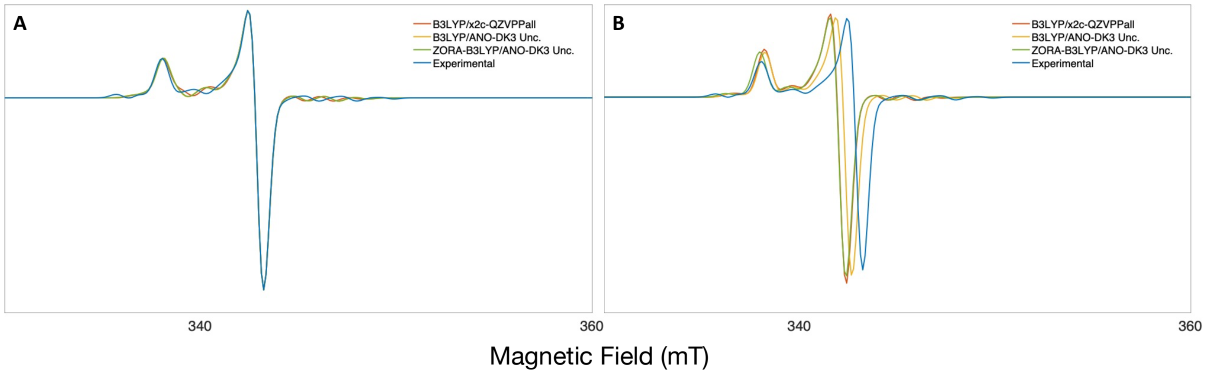

Figure S5. Simulated cw-EPR spectra of [CpTi(cot)] using EasySpin version 6.0. **A.** Comparison between computed and experimental hyperfine coupling constants setting experimental g-values. **B.** Comparison between computed and experimental EPR parameters.

S5. Hyperfine Coupling Decomposition

Table S15. Molecular orbital (MO) nucleus spin density contributions for compounds **1–5**. All calculations have been performed using an uncontracted version of ANO–DK3, B3LYP functional and ZORA relativistic treatment.

Compound	MO	^{a}Spin up (α)	^{a}Spin down (β)	Net Contribution
$[Cu(mnt)_2]^{2-}$	0 (1s)	10448.709928	-10448.724063	-0.014135
	5 (2s)	987.518789	-987.979931	-0.461142
	37 (3s)	144.188654	-143.846839	0.341815
	67 (valence)	0.161240	0.175200	-0.01396
	70 (valence)	0.605247	0.00000	0.605247
	71 (valence)	0.000000	-0.729916	-0.729916
	75 (valence)	0.000000	-0.075463	-0.075463
	78 (valence)	1.615801	-1.603239	0.012562
$[V(dmit)_3]^{2-}$	0 (1s)	4502.639159	-4502.644249	-0.005090
	16 (2s)	396.445869	-369.903024	-0.457155
	89 (3s)	54.925780	-54.769801	0.155979
	108 (valence)	0.195342	0.177957	0.017385
	117 (valence)	0.403931	0.355959	0.047972
	123 (valence)	0.251606	0.238234	0.013372
	138 (valence)	0.034361	0.010272	0.024089
	141 (valence)	0.939877	0.967312	-0.027435
	146 (valence)	0.021944	0.000005	0.021939
	148 (valence)	0.046414	0.000076	0.046338
$[V(C_8S_8)_3]^{2-}$	0 (1s)	4502.627895	-4502.632244	-0.004349
	25 (2s)	396.468339	-396.869749	-0.401410
	149 (3s)	54.954160	-54.812086	0.142074
	183 (valence)	0.187306	-0.175321	0.011985
	191 (valence)	0.027886	-0.017480	0.010406
	206 (valence)	0.065093	-0.006613	0.05848
	207 (valence)	0.011189	-0.046762	-0.035573
	209 (valence)	0.025606	-0.015535	0.010071
	219 (valence)	0.122479	-0.088172	0.034307
	222 (valence)	0.136319	-0.100649	0.03567
	223 (valence)	0.045072	-0.108819	-0.063747
	247 (valence)	0.109832	-0.003168	0.106664
	249 (valence)	0.135940	-0.024933	0.111007
	250 (valence)	0.000975	-0.015337	-0.014362
	251 (valence)	0.587423	-0.533436	0.053987
	252 (valence)	0.007914	-0.330686	-0.322772
	255 (valence)	0.016752	-0.004180	0.012572

	256 (valence)	0.043594	-0.005455	0.038139
	257 (valence)	0.040540	-0.000732	0.039808
	270 (valence)	0.012393	-0.001820	0.010573
$[VO(dmit)_2]^{2-}$	0 (1s)	4502.612219	-4502.615754	-0.003535
	11 (2s)	396.479722	-396.839240	-0.359518
	62 (3s)	54.757190	-54.623186	0.134004
	83 (valence)	0.149841	-0.128581	0.021260
	87 (valence)	0.177812	-0.162952	0.014860
	98 (valence)	0.386372	-0.534790	-0.148418
	102 (valence)	1.028937	-0.883105	0.145832
	112 (valence)	0.029750	-0.046213	-0.016463
	113 (valence)	0.057775	0.000000	0.057775
CpTi(cot)	0 (1s)	3873.540986	-3873.543185	-0.002199
	1 (2s)	335.768406	-336.027912	-0.259506
	18 (3s)	45.187734	-45.135144	0.05259
	42 (valence)	0.787415	0.742477	0.044938
	48 (valence)	0.027784	0.00000	0.027784
	49 (valence)	0.000000	0.022982	-0.022982
	56 (valence)	0.028570	0.000000	0.02857

[a] Electron density within the nucleus given in a.u.$^{-3}$

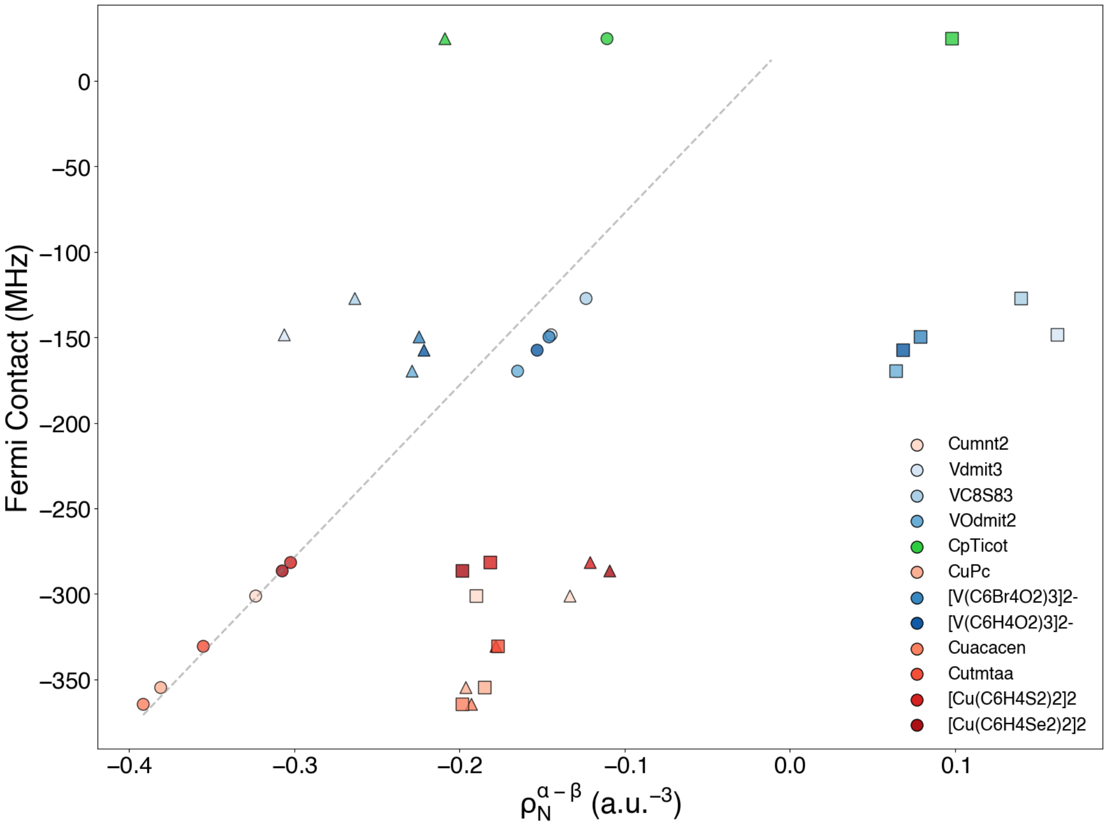

Figure S6. Correlation between isotropic term and nuclear spin density for compounds **1–12** Squares represent valence shell contributions, triangles represent core shell contributions and circles show the total contribution. Calculations were carried out employing B3LYP/ANO – DK3 and using ZORA relativistic treatment.

Table S16. Main axis values of the one-center reduced field gradient integral for all d orbitals in d^1 and d^9 systems (derived from Equation 6).

Orbital	f_{xx}	f_{yy}	f_{zz}
d_{z^2}	$-\frac{2}{7}$	$-\frac{2}{7}$	$\frac{4}{7}$
$d_{x^2-y^2}$	$\frac{2}{7}$	$\frac{2}{7}$	$-\frac{4}{7}$
d_{xy}	$\frac{2}{7}$	$\frac{2}{7}$	$-\frac{4}{7}$
d_{xz}	$\frac{2}{7}$	$-\frac{4}{7}$	$\frac{2}{7}$
d_{yz}	$-\frac{4}{7}$	$\frac{2}{7}$	$\frac{2}{7}$

Table S17. Nucleus spin density contribution per MO for model compounds. All calculations have been performed using an uncontracted version of ANO–DK3, B3LYP functional and ZORA relativistic treatment.

Geometry	V–N (Å)	MO	^{a}Spin up (α)	^{a}Spin down (β)	Net Contribution
Trigonal Plana (C_{3v})	2.046	0 (1s)	4502.881567	-4502.884883	-0.003316
		1 (2s)	396.486006	-396.958045	-0.472039
		8 (3s)	55.426090	-55.248623	0.177467
		21 (Valence)	1.038184	-1.309788	-0.271604
		23 (Valence)	0.364384	-0.141717	0.222667
Vacant Tetrahedra (C_{3v})	2.039	0 (1s)	4502.889341	-4502.891425	-0.002084
		1 (2s)	396.494591	-396.954028	-0.459437
		8 (3s)	55.349062	-55.165414	0.183648
		21 (Valence)	0.000000	-0.914056	-0.914056
		22 (Valence)	0.269175	0.000000	0.269175
		23 (Valence)	1.406725	-0.705276	0.701449
Square Planar (D_{4h})	2.044	0 (1s)	4502.814581	-4502.822431	-0.007850
		1 (2s)	396.443544	-396.848978	-0.405434
		9 (3s)	55.532431	-55.335805	0.196626
		25 (Valence)	1.288550	-1.382685	-0.094135
Tetrahedra (T_d)	2.041	0 (1s)	4502.851152	-4502.852626	-0.001474
		1 (2s)	396.495877	-396.906534	-0.410657
		9 (3s)	55.347576	-55.176533	0.171043
		25 (Valence)	0.000001	-2.084104	-2.084103
		26 (Valence)	2.234185	0.000000	2.234185
Seesaw (C_{2v})	2.043	0 (1s)	4502.828544	-4502.832793	-0.004249
		1 (2s)	396.478098	-396.876716	-0.398618

		9 (3s)	55.451836	-55.288075	0.163761
		25 (Valence)	0.368582	-1.240754	-0.872172
		26 (Valence)	1.598900	0.000000	1.598900
		27 (Valence)	0.000004	-0.659504	-0.659500
Trigonal Bipyramid (D_{3h})	2.130	0 (1s)	4502.836985	-4502.839489	-0.002504
		1 (2s)	396.474058	-396.891429	-0.417371
		10 (3s)	55.394308	-55.219679	0.174629
		29 (Valence)	1.909240	-1.818869	0.090371
		30 (Valence)	0.214384	-0.000562	0.213822
		31 (Valence)	0.000019	-0.150680	-0.150661
Square–Based Pyramid (C_{4v})	2.130	0 (1s)	4502.850230	-4502.852036	-0.001806
		1 (2s)	396.486758	-396.912551	-0.425793
		10 (3s)	55.383352	-55.212341	0.171011
		29 (Valence)	1.901437	-1.817364	0.084073
		30 (Valence)	0.109532	-0.047630	0.061902
Octahedra (O_h)	2.168	0 (1s)	4502.794879	-4502.799909	-0.005030
		1 (2s)	396.453790	-396.842953	-0.389163
		11 (3s)	55.544124	-55.371362	0.172762
		33 (Valence)	2.039398	-1.959323	0.080075
		34 (Valence)	0.037364	-0.009877	0.027487
Trigonal Prism (D_{3h})	2.169	0 (1s)	4502.836799	-4502.839426	-0.002627
		1 (2s)	396.483245	-396.895257	-0.412012
		11 (3s)	55.422486	-55.253644	0.168842
		33 (Valence)	1.859865	-1.749548	0.110317
		39 (Valence)	0.059215	0.000000	0.059215
Pentagonal Bipyramid (D_{5h})	2.220	0 (1s)	4502.828735	-4502.833860	-0.005125
		1 (2s)	396.472667	-396.881226	-0.408559
		12 (3s)	55.419224	-55.250134	0.169090
		37 (Valence)	1.699837	-1.604260	0.095577
		38 (Valence)	0.126792	-0.104168	0.022624
Capped Octahedra (C_{3v})	2.230	0 (1s)	4502.835896	-4502.841555	-0.005659
		1 (2s)	396.482765	396.887559	-0.404794
		12 (3s)	55.419447	55.247795	0.171652
		37 (Valence)	1.779315	-1.667743	0.111572

[a]Electron density within the nucleus given in a.u.$^{-3}$

Table S18. Spin Dipolar Component, SOMO and orbital spatial symmetry for Vanadium model compounds. All calculations have been performed using an uncontracted version of ANO–DK3, B3LYP functional and ZORA relativistic treatment.

Compound	A_{xx}	A_{yy}	A_{zz}	SOMO
Trigonal Planar	106.2	-199.7	93.5	d_{xz}
Vacant Tetrahedra	109.6	96.2	-205.9	d_{xy}
Square Planar	111.4	111.4	-222.8	d_{xy}
Tetrahedra	-104.3	-104.3	208.6	d_{z^2}
Trigonal Bipyramid	105.5	-210.5	104.9	d_{xz}
Square-Based Pyramid	103.8	103.8	-207.6	d_{xy}
Octahedra	108.5	107.3	-215.8	d_{xy}
Trigonal Prism	-111.4	-112.7	225.1	d_{z^2}
Pentagonal Bipyramid	-201.4	115.5	85.9	d_{yz}
Capped Octahedra	107.1	101.1	-208.2	$d_{x^2-y^2}$

Structures were generated using Shapes 2.1 substituting V–N bond lengths for optimized ones from same-numbered ligand optimized compounds.

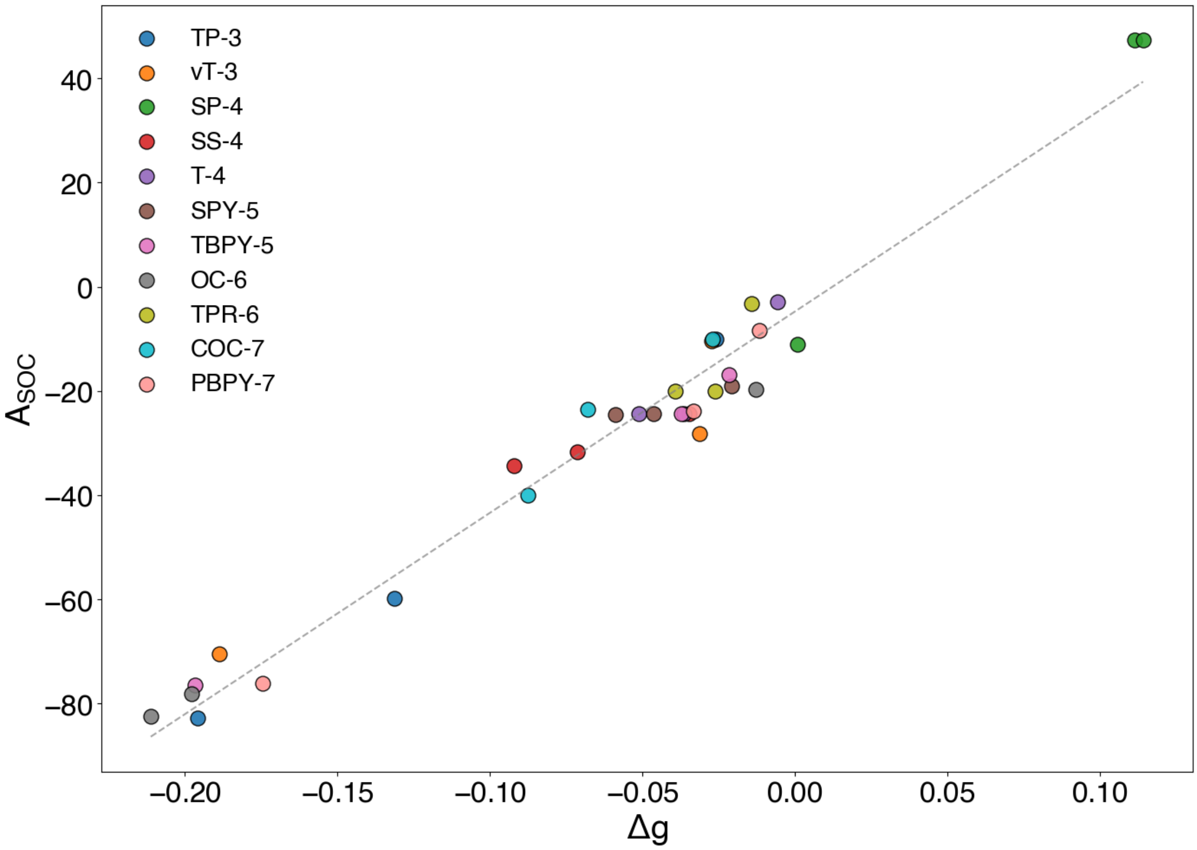

Figure S7. $\Delta g_{\mu\nu}$ against $\mathbf{A}_{\mu\nu}^{SOC}$ (where $\mu = \nu$) for model compounds.